

Multi-Spectral Gaussian Splatting with Neural Color Representation

LUKAS MEYER, JOSEF GRÜN, MAXIMILIAN WEIHERER, BERNHARD EGGER, MARC STAMMINGER, and LINUS FRANKE, Friedrich-Alexander-Universität Erlangen-Nürnberg-Fürth, Germany

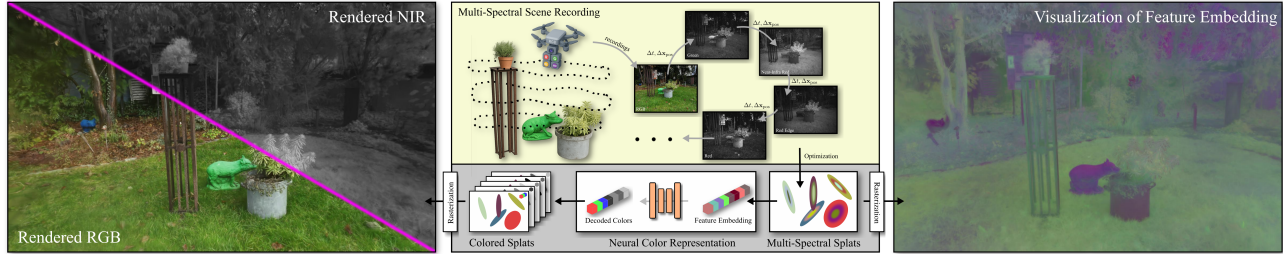


Fig. 1. Our approach, *Multi-Spectral Gaussian Splatting*, is capable of merging multi-spectral images into one representation. To store all spectral bands jointly, we propose a unified neural color representation. We encode spectral data from various bands—red, green, blue, red-edge, and near-infra red—into a per-splat feature embedding. To render individual spectral bands, we train a shallow MLP to decompose the feature embedding into its constituent bands. The left image shows a rendering of RGB and near-infra red, while the right image visualizes the feature embedding. Notice how regions with similar spectral characteristics cluster together in the learned feature space. A video of a visualization can be found here: <https://youtu.be/5AQRJ7Ns9q0>

We present MS-Splatting—a multi-spectral 3D Gaussian Splatting (3DGS) framework that is able to generate multi-view consistent novel views from images of multiple, independent cameras with different spectral domains. In contrast to previous approaches, our method does not require cross-modal camera calibration and is versatile enough to model a variety of different spectra, including thermal and near-infra red, without any algorithmic changes. Unlike existing 3DGS-based frameworks that treat each modality separately (by optimizing per-channel spherical harmonics) and therefore fail to exploit the underlying spectral and spatial correlations, our method leverages a novel neural color representation that encodes multi-spectral information into a learned, compact, per-splat feature embedding. A shallow multi-layer perceptron (MLP) then decodes this embedding to obtain spectral color values, enabling joint learning of all bands within a unified representation. Our experiments show that this simple yet effective strategy is able to improve multi-spectral rendering quality, while also leading to improved per-spectra rendering quality over state-of-the-art methods. We demonstrate the effectiveness of this new technique in agricultural applications to render vegetation indices, such as normalized difference vegetation index (NDVI).

1 INTRODUCTION

The rise of recent (neural) rendering techniques such as Neural Radiance Fields (NeRFs) [Mildenhall et al. 2020] and 3D Gaussian Splatting (3DGS) [Kerbl et al. 2023] has transformed reconstruction and interaction with 3D scenes in the *visible* light spectrum. However, spectral bands beyond the visible spectrum can enhance the prevailing geometric or appearance details [Albanwan et al. 2024; Anuta 1970]. To uncover and exploit these hidden aspects, incorporating more than three spectral bands (i.e., beyond conventional RGB) into scene representations is the next crucial step.

Authors’ address: Lukas Meyer, lukas.meyer@fau.de; Josef Grün, josef.m.gruen@fau.de; Maximilian Weiherer, maximilian.weiherer@fau.de; Bernhard Egger, bernhard.egger@fau.de; Marc Stamminger, marc.stamminger@fau.de; Linus Franke, linus.franke@fau.de, Friedrich-Alexander-Universität Erlangen-Nürnberg-Fürth, Erlangen, Germany.

The increasing affordability of multi-spectral and thermal cameras—both, airborne and handheld—enabled widespread adoption in agriculture and forestry [Huang et al. 2020], environmental surveying, and industrial inspection [Wilson et al. 2023]. Consequently, recent years have seen a surge of work combining neural rendering with multi-modal data from (possibly independent) cameras covering different spectral bands; specifically, emission modalities such as thermal cameras [Hassan et al. 2024; Lin et al. 2024b; Lu et al. 2024a; Özer et al. 2024], and reflectance modalities such as multi-spectral or hyper-spectral devices [Chen et al. 2024a; Li et al. 2024b; Poggi et al. 2022; Sinha et al. 2024; Thirgood et al. 2024].

Existing 3DGS variants adapted to spectra other than RGB [Li et al. 2024b; Lu et al. 2024a] treat different spectral bands in isolation, encoding each band into *separate* spherical harmonics. While this is a natural and straightforward extension, it prevents the model from exchanging information *across* different spectra. Additionally, they mainly assume shared camera parameters between various sensors; hence, rely on tedious cross-modal camera calibration to accurately align RGB, near-infra red, thermal, or images from other modalities.

In this work, we propose *Multi-Spectral Gaussian Splatting* (MS-Splatting) to tackle these two shortcomings. In contrast to previous work, our method does not assume shared camera parameters between different sensors and can therefore be applied to images captured from fully independent cameras without fixed or even known relative positions. As a result, MS-Splatting inherently handles spatially and/or temporally misaligned images, neither requiring alignment of images after data acquisition nor explicit cross-modal camera calibration. Moreover, we replace spherical harmonics and present a new *neural color representation* that jointly learns all spectral bands within a *single* representation, effectively enabling spectral cross-talk to reinforce information across different spectral domains. To do so, we first encode all spectral bands into a per-splat feature embedding and then decode it via a lightweight,

view-conditioned multi-layer perceptron (MLP) that directly predicts view-dependent colors.

Our evaluation shows that the proposed approach outperforms state-of-the-art methods ThermalGaussian [Lu et al. 2024a] and ThermoNeRF [Hassan et al. 2024] in jointly learning multiple spectral bands. Furthermore, we demonstrate that MS-Splatting matches the performance of specialized pipelines developed for emission modalities such as thermal imaging, indicating that our method is versatile enough to represent a variety of different spectra *without* any algorithmic changes. Lastly, we not only improve per-spectrum rendering quality but also exceed 3DGS on RGB novel view synthesis, showing that RGB profits from multi-spectral data. In summary, our key contributions are as follows:

- We introduce MS-Splatting, a multi-spectral neural scene representation based on 3DGS that does not require cross-spectral camera calibration.
- We propose a novel *neural color representation* that efficiently encodes multiple spectral bands into a joint representation shared across different spectra, therefore optimally exploiting cross-spectral color properties.
- We are the first to compute vegetation indices using novel view synthesis.
- We release both, the code and the multi-spectral dataset soon.

2 RELATED WORK

2.1 Novel View Synthesis and Radiance Fields

Methods for novel view synthesis historically build on image-based rendering [Shum and Kang 2000; Shum et al. 2008], whereby images are warped onto a geometry proxy obtained through active depth measuring or Structure-from-Motion [Schönberger and Frahm 2016; Snavely et al. 2006] and multi-view stereo [Goesele et al. 2007; Schönberger et al. 2016]. Recent advances in neural rendering [Tewari et al. 2020, 2022] allow direct entangling of 3D reconstruction and rendering through differentiable rendering. NeRFs [Mildenhall et al. 2020] optimize a 3D volume abstracted in an MLP, sparsing a field with many subsequent quality and speed increases [Barron et al. 2021, 2022, 2023; Müller et al. 2022; Zhang et al. 2020].

Recently, point-based approaches proved to be a great alternative in the speed-to-quality tradeoff, first represented through point sample or splat rendering with neural filtering [Aliev et al. 2020]. Thereby, high-dimensional per-point features are optimized for each point of a geometry proxy to capture the local appearance and decoded with a CNN [Franke et al. 2023, 2024; Harrer et al. 2023; Kopanas et al. 2021; Rakhimov et al. 2022; Rückert et al. 2022] or an MLP [Kopanas et al. 2022]. We draw inspiration from these approaches, as we optimize high-dimensional appearance features per primitive to capture multi-spectral appearances and radiance; however, we specifically use this as a scheme to unify appearance channels.

3D Gaussian Splatting (3DGS) [Kerbl et al. 2023] revolutionized point-based radiance field rendering by representing points as 3D Gaussian distributions $G(\mathbf{x}) = e^{-\frac{1}{2}(\mathbf{x}-\boldsymbol{\mu})^T \boldsymbol{\Sigma}^{-1}(\mathbf{x}-\boldsymbol{\mu})}$, with position $\boldsymbol{\mu}$ and covariance $\boldsymbol{\Sigma}$, and omitting neural components entirely. Rendering is done with alpha blending $C = \sum_{i \in N} c_i \alpha_i T_i$,

with $T_i = \prod_{j=1}^{i-1} (1 - \alpha_j)$ for each pixel with all contributing Gaussians N with colors c . Notably, colors are hereby stored in spherical harmonics with three bands.

Subsequent works improved performance [Hahlbohm et al. 2025; Kheradmand et al. 2024; Niemeyer et al. 2024; Radl et al. 2024; Yu et al. 2024], compression [Bagdasarian et al. 2024; Niedermayr et al. 2024], scalability [Kerbl et al. 2024; Lin et al. 2024a] and dynamic scenes [Luiten et al. 2024; Wu et al. 2024a]; however, the original algorithm remains remarkably consistent in reconstruction quality. We refer to recent surveys for more details [Chen and Wang 2024; Dalal et al. 2024; Fei et al. 2024; Wu et al. 2024b].

FeatSplat [Martins and Civera 2024] is methodologically closest to our approach. They learn a feature vector per splat that encodes both color and semantic information. However, rather than alpha-blending splat colors, they “splat” these feature vectors onto the image pixels and then decoded with an MLP that predicts both the pixel’s color and its semantic label. Furthermore, their method does not allow for multiple different spectral bands.

2.2 Multi-Modal Novel View Synthesis

Multi-modal approaches combine different sensing modalities such as passive reflectance (multi-spectral), passive emission (thermal), or active illumination (LiDAR or radar). In this paper, we focus only on passive reflectance and thermal emission. In contrast, single-modal methods operate on a single sensing modality. Both, multi-spectral and hyper-spectral imaging, fall under this umbrella, differing only in spectral resolution: multi-spectral sensors capture roughly 4–10 discrete channels, whereas hyper-spectral cameras sample hundreds of narrower bands up to about 600 continuous channels spanning 400 nm to 2500 nm [Adam et al. 2010].

The integration of RGB and thermal imaging for novel view synthesis is gaining popularity. ThermalNeRF [Lin et al. 2024b] and Xu et al. [2025] use thermal data to enhance low-light reconstruction, with the latter also improving RGB through thermal cues. Ye et al. [2024b] focus on thermal input training alone, while Özer et al. [2024] assess various NeRF architectures to find optimal multi-modal configurations across thermal, near-infra red, and depth. Both ThermoNeRF [Hassan et al. 2024] and Thermal-NeRF [Ye et al. 2024b] utilize dual neural fields for RGB and thermal synthesis. In the 3DGS realm, Thermal3D-GS [Chen et al. 2024b] pioneered thermal-only splatting. ThermalGaussian [Lu et al. 2024b] builds on this by combining RGB and thermal splats. They employ spherical harmonics for *separate* color modeling.

Recent advances have explored the integration of multi- and hyper-spectral imagery into neural scene representations. X-NeRF [Poggi et al. 2022] introduces a cross-modal neural field that jointly models RGB, multi-spectral, and near-infra red bands, learning camera extrinsics during optimization rather than relying on pre-calibration. Similarly, Spec-NeRF [Li et al. 2024a] captures separate visible-spectrum bands while simultaneously estimating each camera’s spectral sensitivity functions to enable accurate reconstruction. SpectralNeRF [Li et al. 2024b] takes a different approach by training on eleven discrete spectral channels to predict per-band spectral maps, which are then fused into high-quality RGB images using a

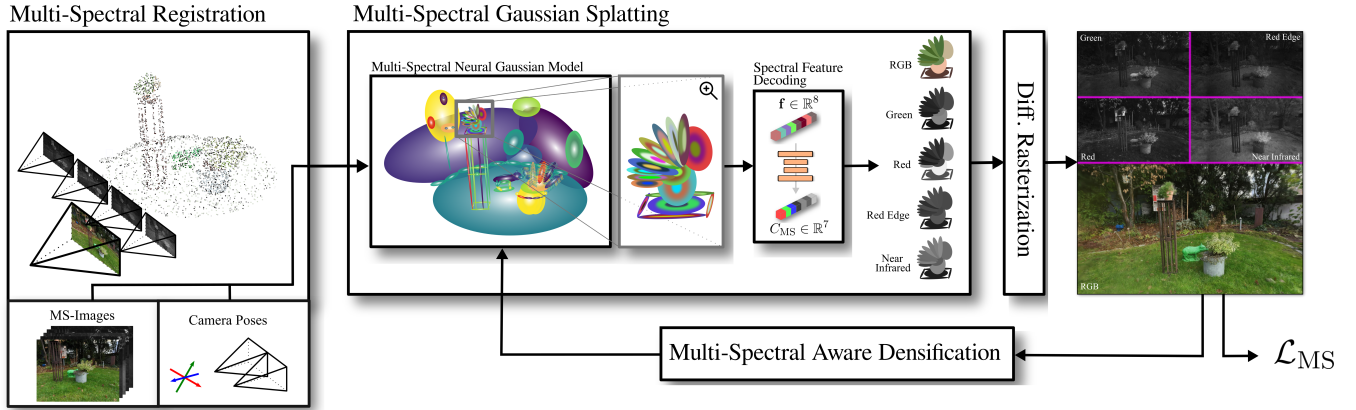


Fig. 2. Overview of MS-Splatting pipeline. After initial Structure-from-Motion Registration across all channels simultaneously, we initialize a multi-spectral neural Gaussian model shared for all spectral channels. Thereby, colors of all spectral bands are encoded in a per-splat feature vector and decoded with a tiny MLP. During optimization, the shared Gaussian model and per Gaussian features are optimized by drawing a random view and spectral band under a multi-spectral loss formulation.

U-Net-style architecture. Extending to hyper-spectral data, Hyper-spectral NeRF [Chen et al. 2024a] embeds continuous wavelength information directly into its radiance field, allowing for detailed, per-wavelength radiance predictions across more than 128 channels. HyperGS [Thirgood et al. 2024] further abstracts the spectral domain by compressing high-dimensional hyper-spectral inputs into a latent space via a pre-trained autoencoder; during training, Gaussian splats learn latent spectral signatures that a view-conditioned MLP transforms into view-dependent spectral and opacity features, which are decoded back into full spectra at rendering time. SpectralGaussians [Sinha et al. 2024] augments the 3DGS framework with a physically-based shading model that estimates per-spectrum reflectance and illumination parameters for each Gaussian, enabling

more accurate and physically grounded spectral rendering. Collectively, these methods demonstrate the potential of neural rendering techniques to capture and reconstruct complex spectral phenomena.

In contrast to all these methods, our approach is the first to use a neural color representation to jointly optimize all spectral bands simultaneously. As we show in the results, this approach leads to superior performance in the reconstruction of multi-spectral scenes.

3 METHOD

The input to our method comes from a set of n cameras, C_j . Each of these cameras has its own intrinsic parameters and covers one or multiple (spectral) bands. We record images with all these cameras with independent trajectories, resulting in a dataset of n sets, $\mathcal{I} = \{I_1, I_2, \dots, I_n\}$, where I_j contains images captured from camera C_j . In this work, we use $n = 5$ cameras: an RGB camera, and four multi-spectral cameras capturing red (R), green (G), red edge (RE), and near-infra red (NIR).

Based on the input images, we optimize a 3DGS-based scene representation which allows for novel view synthesis across multiple spectral bands. Our framework operates in two stages: In the first step (Section 3.1), we compute camera poses and a sparse point cloud from \mathcal{I} using classical Structure-from-Motion (SfM) (COLMAP) [Schönberger and Frahm 2016] *without* assuming shared camera parameters across multiple sensors. Then, in the second stage (Section 3.2), we use previously computed poses and point cloud to initialize and train the unified neural color representation within our multi-spectral Gaussian Splatting model, which, eventually, yields a compact multi-spectral scene representation.

3.1 Multi-Spectral Camera Calibration

Existing multi-spectral and multi-modal scene representations [Lin et al. 2024b; Lu et al. 2024a; Özer et al. 2024] usually assume *shared* camera parameters (intrinsic *and* extrinsic) across multiple channels, and hence need some form of cross-modal camera calibration to superimpose images captured using different sensors. Once aligned, camera parameters are obtained by applying SfM only to the RGB



Fig. 3. Exemplary SIFT [Lowe 1999] (as used by COLMAPs SfM [Schönberger and Frahm 2016]) feature matching between RGB, red and near-infra red channel. For visualization purpose only the best 6 matches are depicted.

images. Although simple, this workflow requires either a fixed setup and special hardware for camera calibration, or the use of error-prone methods to precisely align RGB and multi-spectral images after they have been captured.

In this work, we present a new and simple approach that neither assumes shared camera intrinsics nor extrinsics across multiple bands, allowing for images to be captured from different viewpoints and/or points in time. Specifically, we found that processing all images in \mathcal{I} with SfM *at once* leads to satisfying results if we use separate, per-camera intrinsics. This works because multi-spectral and RGB images show about the same high-frequency geometric details when having a comparable spatial resolution [Irani and Anandan 1998] (as the case for most commercially available multi-spectral cameras). Since all cameras see the same geometric details, sophisticated SfM’s feature detection (e.g., using SIFT [Lowe 1999]) and matching is well applicable to match RGB and multi-spectral features *across spectral bands*. Please see Fig. 3 for an illustration.

To the best of our knowledge, our method is the first to work with spatially and/or temporally unaligned images and, therefore, is perfectly suited to be applied with dynamic recordings behavior.

3.2 Multi-Spectral Gaussian Splatting

Similar to previous works, our method represents all available channels (RGB and multi-spectral) within a *single* 3DGS model. To this end, we assume a *shared geometry* for all bands, but, unlike previous approaches, model color values within a single *neural color representation* instead of per-band spherical harmonics, effectively enabling information to be shared across multiple channels. Fig. 2 provides an overview of our pipeline.

3.2.1 Neural Color Representation. Our key insight is that RGB and multi-spectral channels profit from exchanging information between each other instead of being treated separately. To implement this finding, we replace traditional spherical harmonics and predict colors $\hat{c}_i \in \mathbb{R}^B$ directly using a shallow MLP:

$$\hat{c}_i = \text{MLP}(f_i \circ \mathbf{d}; \Theta), \quad (1)$$

where $f_i \in \mathbb{R}^d$ denotes a trainable, per-splat feature vector that compactly encodes color information across all bands, and $\mathbf{d} \in \mathbb{S}^2$ is the normalized viewing direction. $B = \sum_{j=1}^n B_j$ denotes the total number of bands, where B_j is the number of channels per camera (in our case, $B = 7$; three RGB channels, and four multi-spectral). Θ are the learnable parameters of the MLP, and \circ denotes vector concatenation.

To render the individual colors of each spectral band we follow the default 3DGS rasterization pipeline.

3.2.2 Loss Function. We employ the following loss function to train our model:

$$\mathcal{L}_{\text{MS}} = \sum_{I_j \sim \mathcal{I}} \sum_{I \sim \mathcal{I}_j} \mathcal{L}_{\text{3DGS}}(\hat{I}, I) + \lambda_{\text{norm}} \sum_{i=1}^m (\|f_i\|_2 - 1)^2, \quad (2)$$

where I denotes a randomly chosen image from the set \mathcal{I}_j of all images captured using the j -th camera, and \hat{I} is the corresponding rendered image. $\mathcal{L}_{\text{3DGS}}$ is the standard 3DGS loss,

$$\mathcal{L}_{\text{3DGS}}(\hat{I}, I) = (1 - \lambda) \mathcal{L}_1(\hat{I}, I) + \lambda \mathcal{L}_{\text{SSIM}}(\hat{I}, I). \quad (3)$$

The second term in Eq. (2) regularizes the per-splat feature vectors, where m denotes the total number of splats in the scene. We back-propagate this loss through our model to update the parameters of the MLP, Θ , feature vectors, f_i , as well as the conventional 3DGS parameters, $\{\mu, \Sigma, \sigma, \mathbf{s}\}$.

3.2.3 Multi-Spectral Aware Densification. We utilize the Gaussian densification strategy first introduced by [Kerbl et al. 2023] and later refined by [Ye et al. 2024a], but adapt it to better respond to multi-spectral input data. In every iteration, for every rendered Gaussian G_i , we calculate the homodirectional view-space positional gradient

$$\hat{g}_i^{(j)} = \left(\sum_{k=1}^m \left| \frac{\partial L_k}{\partial \mu_{i,x}^{(2d)}} \right|, \sum_{k=1}^m \left| \frac{\partial L_k}{\partial \mu_{i,y}^{(2d)}} \right| \right), \quad (4)$$

where $j \in [n] := \{1, 2, \dots, n\}$, $\mu_i^{(2d)}$ is the view-space position of G_i , m is the number of pixels rendered for the Gaussian, and L_k is the loss function in Eq. (2) computed for the k -th pixel. We choose a densification interval of 300 iterations, during which the calculated $\hat{g}_i^{(j)}$ are accumulated. In the next densification step, if the criterion

$$\max_{j \in [n]} \left(\frac{\sum \|\hat{g}_i^{(j)}\|}{n^{(j)}} \right) > \tau_{\text{grad}} \quad (5)$$

is met for a Gaussian, we split or clone it according to the approach laid out by [Kerbl et al. 2023], where $n^{(j)}$ is the number of view-space gradients accumulated in the densification interval for the current band. We choose $\tau_{\text{grad}} = 0.0008$ in our experiments.

Note that we separately accumulate view-space gradients for each spectral band, and then select the maximum average gradient for the densification criterion. Since high view-space gradients correlate with under- or over-reconstructed areas of the scene [Kerbl et al. 2023], this approach recognizes when a region is properly modeled for one spectral band, but is insufficiently reconstructed for another, and introduces new Gaussians to the area accordingly. Therefore, our modification to the densification strategy allows for proper reconstruction of high-frequency details that are only visible in one or few of the captured spectral bands. Table 3 evaluates our method compared to the default densification strategy on our multi-spectral datasets.

3.3 Implementation Details

Our model builds upon *gsplat* [Ye et al. 2025] and is implemented within the *Nerfstudio* [Tancik et al. 2023] framework.

3.3.1 Training Strategy. We trained our model for 120,000 iterations using the Adam optimizer with a learning rate of 0.005. Since the per-point colors of the sparse SfM point cloud contain a mixture of RGB and multi-spectral gray values (due to our combined reconstruction strategy, see Section 3.1), we decided against using them for initialization of our 3DGS model. Instead, we freeze the covariance, mean, scaling, and opacity for the first 500 iterations and let solely the neural colors optimize by only training the feature vectors and MLP parameters. This effectively recovers per-channel color values and successfully prevents our model from large, color-induced gradients which would cause the initial splat positions to

Table 1. Results over all our seven datasets. See also Figs. 6, 7, 8 and Fig. S.F2, S.F3, S.F4, and S.F5 in the supplements for visual comparison. The colors indicate **best** and **second best**. Depending on the method, we train with warped multi-spectral images (W), or the original dataset (O) with independent camera positions. ThermalGaus. (W) uses the original implementation by [Lu et al. 2024a], whereas ThermalGaus. (O) uses our re-implementation described in the supplementary Sec. S4.

	PSNR (\uparrow)						SSIM (\uparrow)						LPIPS (\downarrow)					
	All	RGB	G	R	RE	NIR	All	RGB	G	R	RE	NIR	All	RGB	G	R	RE	NIR
ThermalGaus. (W)	23.55	19.81	23.99	25.66	23.78	24.49	0.699	0.565	0.710	0.763	0.717	0.743	0.342	0.371	0.336	0.305	0.336	0.362
ThermoNeRF (W)	18.91	15.39	19.48	20.62	18.78	20.26	0.500	0.255	0.542	0.616	0.514	0.575	0.606	0.723	0.591	0.554	0.593	0.568
3DGS (O)	23.62	20.86	22.92	25.23	23.33	25.75	0.721	0.623	0.667	0.769	0.730	0.815	0.334	0.283	0.371	0.349	0.331	0.336
ThermalGaus. (O)	24.18	20.17	24.04	26.09	24.14	26.50	0.718	0.564	0.695	0.788	0.732	0.814	0.344	0.387	0.369	0.314	0.341	0.308
Ours (O)	25.65	21.17	25.42	27.79	25.79	28.13	0.763	0.633	0.729	0.827	0.780	0.849	0.266	0.306	0.293	0.240	0.257	0.232

jump around. Feature vectors are initialized from a zero-mean normal distribution with a standard deviation of 0.2. We set $\lambda = 0.2$ and $\lambda_{\text{norm}} = 0.1$, and evaluate our loss function in Eq. (2) only with a *single* randomly chosen image per iteration.

3.3.2 Network Implementation. We use a shallow 3-layer MLP with one hidden layer of dimension 32. We apply exponential linear unit (ELU) activations [Clevert et al. 2015] to all layers except the output, which uses a sigmoid activation to constrain outputs between $[0, 1]$.

4 EVALUATION

We compare our method against current state-of-the-art approaches to confirm the effectiveness of our neural color representation and to show that our framework can be readily extended to data from additional modalities, such as thermal. Moreover, in Sec. 5, we demonstrate (i) how MS-Splatting can be used to compute vegetation indices for agriculture applications, and (ii) how to leverage our learned feature embedding to perform multi-spectral segmentation.

4.1 Multi-Spectral Dataset

We recorded our own dataset comprising seven outdoor scenes as no suitable outdoor multi-view dataset with multi-spectral imagery was available. Voynov et al. [2023] provide an indoor multi-sensor dataset containing RGB, near-infra red, and depth data; Poggi et al. [2022] offer an unposed, forward-facing dataset with RGB, multi-spectral, and near-infra red channels (16 scenes, 10 bands), although they estimate poses by learning relative sensor transformations, which lies outside the scope of our work. Finally, Hyperspectral NeRF [Chen et al. 2024a] captured an indoor hyperspectral dataset of eight scenes with 128 bands, which is not yet publicly released.

For our recordings, we used the DJI Mavic 3M drone [DJI 2025], featuring a dual-camera system: one RGB sensor and four multi-spectral cameras that cover the red (R), green (G), red-edge (RE), and near-infra red (NIR) bands. While the green and red bands overlap with the RGB spectrum, their narrow capture bandwidth (32 nm) provides higher spectral precision. We note that spectral bands can only be captured sequentially—due to hardware restrictions—which can introduce spatial and temporal misalignment, especially in dynamic scenes and due to the drone’s stabilization system. Figure S.F1 illustrates a typical misalignment caused by this sequential capture.

Our dataset includes 360° panoramas of a garden, a dormant cherry tree, an apple orchard during bud swelling, and a lake with a construction trailer; 180° views of a house with solar panels; forward-facing sequences of an apple orchard at harvest; and a top-down survey of a golf course. An overview of the datasets can be seen in

the evaluation images in the supplements. RGB images are captured with a focal length of 24 mm, while each multi-spectral camera has a focal length of 25 mm.

To evaluate methods such as ThermalGaussian [Lu et al. 2024a] and ThermoNeRF [Hassan et al. 2024] which assume shared camera parameters across all spectral bands and are therefore not directly applicable to our dataset, we first superimpose RGB and multi-spectral images by estimating pairwise homographies between each of them (i.e., between RGB + R, RGB + G, RGB + RE, and so on). We then warp multi-spectral images into the RGB frames. Due to focal-length differences, however, the warped multi-spectral images exhibit black borders; we, therefore, crop all images to 1800px×1350px to effectively remove these margins. We trained our model on the original, unaligned data, but cropped images to the same regions to ensure fair comparison.

4.2 Comparison on Multi-Spectral Data

We compare our method against three open-source baselines: ThermalGaussian [Lu et al. 2024a], ThermoNeRF [Hassan et al. 2024], and vanilla 3DGS [Kerbl et al. 2023]. We trained ThermalGaussian and ThermoNeRF four times, pairing RGB with one additional multi-spectral band per run. For vanilla 3DGS, which cannot optimize more than one spectral band at a time, we conducted five independent runs (one per band). Finally, we also re-implemented ThermalGaussian’s “One Multi Modal Gaussian” (OMMG) variant within our framework. However, our implementation extends each splat with extra spherical harmonics to handle multiple (i.e., not just one as in the original implementation) spectral bands simultaneously. More implementation details can be found in the supplements. A comparison to other multi-spectral methods was, due to non-availability of source code, not possible.

Tab 1 presents the results, averaged over all scenes. RGB metrics for ThermalGaussian and ThermoNeRF were computed by averaging respective results over the four runs. As seen, our approach achieves the best overall PSNR, SSIM, and LPIPS: improving PSNR by over 1.4 dB, increasing SSIM by 6 %, and reducing LPIPS by 23 % compared to the previous state-of-the-art ThermalGaussian. Notably, even on RGB data alone, our method outperforms vanilla 3DGS in PSNR and SSIM, demonstrating the cross-spectral benefit of incorporating additional bands. Visual comparisons for all spectral channels are shown in Figs. 6, 7, 8, S.F3 and S.F5. Per-scene results are provided in the supplements.

Table 2. Average performance across six thermal scenes from the ThermalMix dataset [Özer et al. 2024] and the dataset from ThermoNeRF [Hassan et al. 2024]. Detailed information can be seen in the supplements.

Method	PSNR (\uparrow)		SSIM (\uparrow)		LPIPS (\downarrow)	
	RGB	T	RGB	T	RGB	T
ThermalGaussian	24.91	31.34	0.824	0.931	0.226	0.107
ThermoNeRF	16.54	22.45	0.546	0.765	0.376	0.295
Ours	26.31	31.18	0.883	0.934	0.166	0.104
Ours + $\mathcal{L}_{\text{smooth}}$	26.66	31.23	0.892	0.935	0.157	0.095

4.3 Comparison on Multi-Modal Data

We also compared the original implementations of ThermalGaussian [Lu et al. 2024a] and ThermoNeRF [Hassan et al. 2024] against our method on thermal data. To do so, we selected three scenes from the ThermalMix dataset [Özer et al. 2024] and three scenes from the dataset used in ThermoNeRF [Hassan et al. 2024] (details can be found in the supplementary). We evaluated our approach using the same configuration as in Sec. 4.2. Additionally, we tested the influence of the smoothness loss $\mathcal{L}_{\text{smooth}}$ introduced by [Lu et al. 2024a] on our method (see supplements).

The averaged results across all scenes are presented in Tab. 2, with per-scene details provided in the supplementary material. As shown, our approach outperforms both, ThermalGaussian and ThermoNeRF, demonstrating that MS-Splatting generalizes to other modalities without further adaptation. Here, the datasets do provide calibrated pairs of thermal and RGB images and we used the provided camera parameters for all methods.

4.4 Ablation

In this section, we evaluate the impact of our key design choices. Specifically, we assess the new densification strategy (Sec. 4.4.1) and the effect of the dimension of the feature embedding (Sec. 4.4.2). Additional ablations can be found in the supplements.

4.4.1 Densification Strategy. To evaluate our new multi-spectral densification strategy, we compared the standard 3DGS against our *Multi-Spectral Aware Densification* strategy in Tab. 3. From the results shown, we conclude that our new densification strategy slightly improves our overall performance and peaks at a densification interval of 300. The larger interval compared to 3DGS can be attributed to the average being accumulated over multiple steps to compute the gradient correctly.

Table 3. Comparison of densification strategy with alternating densification intervals. 3DGS (*Default*) uses an interval of 100 iterations.

Split Interval	PSNR (\uparrow)	SSIM (\uparrow)	LPIPS (\downarrow)
<i>Default</i> - 100	25.02	0.748	0.310
<i>Default</i> - 200	25.02	0.748	0.317
<i>Default</i> - 300	25.08	0.748	0.319
<i>Default</i> - 400	24.93	0.749	0.320
<i>Default</i> - 500	24.86	0.747	0.323
Ours - 100	24.93	0.750	0.267
Ours - 200	25.08	0.754	0.271
Ours - 400	25.09	0.757	0.275
Ours - 300	25.16	0.758	0.271
Ours - 500	24.85	0.756	0.281

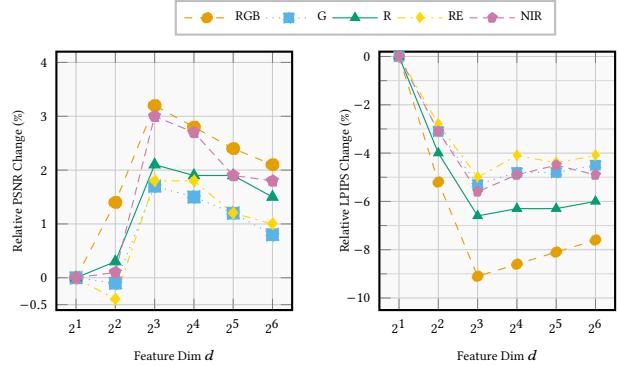


Fig. 4. Relative changes in PSNR and LPIPS for the lightweight MLP and with varying feature-embedding dimension d .

4.4.2 Feature Dimension. To isolate the effect of the feature embedding dimension, we swept this parameter while keeping the MLP architecture fixed (one hidden layer of width 32). Figure 4 shows the relative change in PSNR and LPIPS (SSIM follows a similar trend with smaller fluctuations) as functions of the embedding size d . The results indicate that a shallow MLP with $d = 8$ yields the best overall performance. Notably, even $d = 2$ provides sufficient capacity to encode substantial information across all input bands.

5 AGRICULTURE APPLICATIONS

For MS-Splatting, we regard the agricultural domain as the most promising field of application. Novel view synthesis has recently been adopted in the agricultural domain, with applications ranging from horticulture [Chopra et al. 2024; Meyer et al. 2024a,b], to greenhouse monitoring [Choi et al. 2024; Smitt et al. 2023; Zheng et al. 2024], in-field crop observation [Baar et al. 2024; Esser et al. 2023; Yang et al. 2024], and laboratory-based plant phenotyping [Ojo et al. 2024; Saeed et al. 2023].

We place particular emphasis on computing various vegetation indices, as discussed in Sec. 5.1. Additionally, we tested clustering the feature space to enable semantic segmentation based on their spectral feature composition in Sec. 5.2.

5.1 Vegetation Indices

Vegetation Indices (VI) are a spectral imaging transformation designed to quantify vegetation type, plant mass, and health in a scene [Jackson and Huete 1991]. When light penetrates a surface, it is partly reflected, absorbed, or transmitted depending on the material and wavelength. Soil typically absorbs and reflects visible wavelengths while only little light is being transmitted, whereas vegetation absorbs most viable light but strongly reflects and transmits near-infra red wavelengths. This pronounced NIR reflectance arises from the internal leaf’s structure, which efficiently scatters light [Jackson and Huete 1991].

Consequently, many vegetation indices, such as the normalized difference vegetation index (NDVI), the green NDVI (GNDVI), and the soil-adjusted vegetation index (SAVI), all exploit the strong NIR reflectance of vegetation. In the simplest form, NDVI is computed

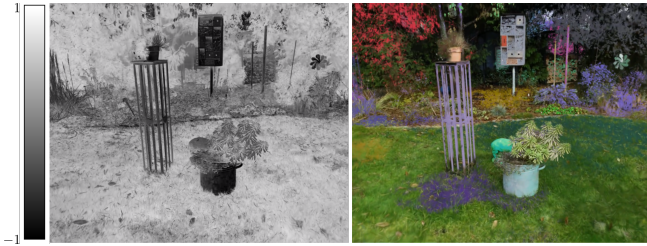


Fig. 5. (Left) NDVI computed by synthesizing the red and near-infra red channels via MS-Splatting. Values between -1 and 0 indicate inanimate object, 0 to 0.33 diseased, 0.33 to 0.66 moderately healthy and 0.66 to 1 very healthy plants. (Right) Spectral-feature clustering based on the learned per-splat embeddings, with clusters reflecting similar spectral properties.

on a per-pixel basis as

$$\text{NDVI} = \frac{\text{NIR} - R}{\text{NIR} + R}. \quad (6)$$

This formula implicitly assumes that the red and NIR sensors are perfectly co-registered or that the scene distance is large relative to the sensor baseline, as is typically the case for top-down drone or satellite imagery. However, in near-field scenarios (orchards, greenhouses, phenotyping rigs), separate multi-spectral sensors often capture images from slightly different viewpoints and at different time steps. Without precise image registration, even small spatial or temporal misalignment (for example, due to wind or vehicle motion) can introduce significant artifacts, as shown on the left in Fig. S.F1.

As a baseline, we apply mutual information (MI)-based registration, since MI is well known for aligning multi-modal imagery without assuming any specific intensity relationships between channels [Kern and Pattichis 2007; Maes et al. 1997; Zitová and Flusser 2003]. Details are provided in the supplementary material.

To avoid these registration challenges entirely, we exploit our MS-Splatting model for NDVI (and other VI) rendering. While novel view synthesis has not been used previously to compute vegetation indices, a related work trains directly on precomputed NDVI from laboratory hyperspectral scans [Oefelein 2023]. In contrast, our method jointly learns a neural scene representation across all spectral bands, allowing us to render any VI “on the fly” by simply synthesizing the red and NIR images and combining them via Eq. (6). An example NDVI output from MS-Splatting is shown in the left panel of Fig.5.

5.2 Multi-Spectral Segmentation

Another valuable downstream application of MS-Splatting is material-aware surface clustering. By grouping splats whose neural feature embeddings share similar reflectance properties, we can—for example—count fruits, distinguish healthy from diseased vegetation, or segment objects by material type. A nice side effect of our approach is that all of this information is already captured in the learned feature embedding.

To further encourage local consistency, we introduce a cosine-similarity loss between each feature and its spatial neighbors:

$$\mathcal{L}_{\cos}(f_c, \mathcal{F}_s) = \frac{1}{|\mathcal{F}_s|} \sum_{f_s \in \mathcal{F}_s} 1 - \frac{\langle f_c, f_s \rangle}{\|f_c\| \|f_s\|}, \quad (7)$$

where f_c is the center and \mathcal{F}_s is the set of the k nearest neighbors (in Euclidean space). During training, we rebuild the k -NN graph ($k = 16$) after each densification, split, or prune operation. Once training is complete, we extract for each Gaussian splat its 3D position and corresponding feature vector, and then cluster these points using HDBSCAN [McInnes et al. 2017]. Each resulting cluster is visualized to reveal material-consistent regions. An example of this clustering in the Garden scene is shown in Fig. 5 on the right.

6 LIMITATIONS AND FUTURE WORK

One limitation of our work is that, while metrics indicate strong performance, the resulting RGB images can sometimes appear dull. We believe this stems from the fact that both the per-splat feature embeddings and the neural network continue to adapt until the end of training, allowing subtle color shifts from spectral cross-talk to persist. A more in-depth study is needed to understand how the feature-embedding design affects color fidelity.

For future work, it would be valuable to evaluate this framework on truly high-dimensional hyperspectral data. Additionally, following the example of Hyperspectral NeRF [Chen et al. 2024a], learning a continuous per-wavelength representation could enable smooth interpolation between wavelengths and further improve spectral reconstruction. In agricultural settings, a real-time implementation (e.g., LiveNVS [Fink et al. 2023]) or even an immersive multispectral Gaussian splatting system [Franke et al. 2025] could make this use case far more accessible.

7 CONCLUSION

To conclude, we present MS-Splatting, a novel pipeline for view synthesis on multi-spectral images—spanning RGB, green, red, red-edge, and near-infra red bands. At its core lies a unified neural color representation that jointly encodes all spectral channels into a shared feature embedding. A tiny multi-layer perceptron then decodes this embedding to accurately recover each band’s appearance. Our extensive experiments show that this collaboration through a joint feature space leverages both spatial and spectral coherence, yielding consistent cross-spectral improvements across every evaluation metric.

ACKNOWLEDGMENTS

We thank **Martin Hundhausen** for supporting the scene recordings. Lukas Meyer was funded by the 5G innovation program of the German Federal Ministry for Digital and Transport under the funding code 165GU103B. Maximilian Weiherer was funded by the German Federal Ministry of Education and Research (BMBF), FKZ: 01IS22082 (IRRW). The authors are responsible for the content of this publication. The authors gratefully acknowledge the scientific support and HPC resources provided by the Erlangen National High Performance Computing Center (NHR@FAU) of the Friedrich-Alexander-Universität Erlangen-Nürnberg (FAU) under the NHR project *b162dc*. NHR funding is provided by federal and Bavarian state authorities. NHR@FAU hardware is partially funded by the German Research Foundation (DFG) – 440719683.

REFERENCES

- Elhadi Adam, Onesimo Mutanga, and Denis Rugege. 2010. Multispectral and hyperspectral remote sensing for identification and mapping of wetland vegetation: a review. *Wetlands Ecology and Management* 18, 3 (jun 2010), 281–296. <https://doi.org/10.1007/s11273-009-9169-z>
- Hessah Albanwan, Rongjun Qin, and Yang Tang. 2024. Image Fusion in Remote Sensing: An Overview and Meta Analysis. arXiv:2401.08837 [cs.CV] <https://arxiv.org/abs/2401.08837>
- Kara-Ali Aliev, Artem Sevastopolsky, Maria Kolos, Dmitry Ulyanov, and Victor Lempitsky. 2020. Neural Point-Based Graphics. In *European Conference on Computer Vision (ECCV)*. Springer, Springer International Publishing, Cham, 696–712.
- Paul E. Anuta. 1970. Spatial Registration of Multispectral and Multitemporal Digital Imagery Using Fast Fourier Transform Techniques. *IEEE Transactions on Geoscience Electronics* 8, 4 (1970), 353–368. <https://doi.org/10.1109/TGE.1970.271435>
- Stefan Baar, Yosuke Kobayashi, and Shinya Watanabe. 2024. Combining Close Range UAVs and Gaussian Splatting for High-Speed Tomato Leaf Size Estimation and Counting. In *2024 IEEE 13th Global Conference on Consumer Electronics (GCCE)*. 215–218. <https://doi.org/10.1109/GCCE62371.2024.10760832>
- Milena T. Bagdasarian, Paul Knoll, Yi-Hsin Li, Florian Barthel, Anna Hilsman, Peter Eisert, and Wieland Morgenstern. 2024. 3DGS.zip: A survey on 3D Gaussian Splatting Compression Methods. arXiv:2407.09510 [cs.CV]
- Jonathan T. Barron, Ben Mildenhall, Matthew Tancik, Peter Hedman, Ricardo Martin-Brualla, and Pratul P. Srinivasan. 2021. Mip-NeRF: A Multiscale Representation for Anti-Aliasing Neural Radiance Fields. In *Proceedings of the IEEE/CVF International Conference on Computer Vision (ICCV)*. 5855–5864.
- Jonathan T. Barron, Ben Mildenhall, Dor Verbin, Pratul P. Srinivasan, and Peter Hedman. 2022. Mip-NeRF 360: Unbounded Anti-Aliased Neural Radiance Fields. In *Proceedings of the IEEE/CVF Conference on Computer Vision and Pattern Recognition (CVPR)*. 5470–5479.
- Jonathan T. Barron, Ben Mildenhall, Dor Verbin, Pratul P. Srinivasan, and Peter Hedman. 2023. Zip-NeRF: Anti-Aliased Grid-Based Neural Radiance Fields. In *Proceedings of the IEEE/CVF International Conference on Computer Vision (ICCV)*. 19640–19648.
- Gerry Chen, Sunil Kumar Narayanan, Thomas Gautier Ottou, Benjamin Missaoui, Harsh Muriki, Cédric Pradalier, and Yongsheng Chen. 2024a. Hyperspectral Neural Radiance Fields. arXiv preprint arXiv:2403.14839 (2024).
- Guikun Chen and Wenguan Wang. 2024. A survey on 3d gaussian splatting. arXiv preprint arXiv:2401.03890 (2024).
- Qian Chen, shihao Shu, and Xiangzhi Bai. 2024b. Thermal3D-GS: Physics-induced 3D Gaussians for Thermal Infrared Novel-view Synthesis. In *European Conference on Computer Vision*.
- Hong-Beom Choi, Jae-Kun Park, Soo Hyun Park, and Taek Lee. 2024. NeRF-based 3D reconstruction pipeline for acquisition and analysis of tomato crop morphology. *Frontiers in Plant Science* 15 (10 2024). <https://doi.org/10.3389/fpls.2024.1439086>
- Samarth Chopra, Fernando Cladera Ojeda, Varun Murali, and Vijay Kumar. 2024. AgriNeRF: Neural Radiance Fields for Agriculture in Challenging Lighting Conditions. ArXiv abs/2409.15487 (2024). <https://api.semanticscholar.org/CorpusID:272831842>
- Djork-Arné Clevert, Thomas Unterthiner, and Sepp Hochreiter. 2015. Fast and Accurate Deep Network Learning by Exponential Linear Units (ELUs). arXiv: Learning (2015). <https://api.semanticscholar.org/CorpusID:5273326>
- Anurag Dalal, Daniel Hagen, Kjell G. Robbersmyr, and Kristian Muri Knausgård. 2024. Gaussian Splatting: 3D Reconstruction and Novel View Synthesis, a Review. arXiv preprint arXiv:2405.03417 (2024).
- DJI. 2025. Mavic 3 Multispectral (3M). <https://ag.dji.com/mavic-3-m>. Accessed: 2025-01-24.
- Felix Esser, Radu Alexandru Rosu, André Cornelissen, Lasse Klingbeil, Heiner Kuhlmann, and Sven Behnke. 2023. Field Robot for High-Throughput and High-Resolution 3D Plant Phenotyping: Towards Efficient and Sustainable Crop Production. *IEEE Robotics; Automation Magazine* 30, 4 (Dec. 2023), 20–29. <https://doi.org/10.1109/mra.2023.3321402>
- Ben Fei, Jingyi Xu, Rui Zhang, Qingyuan Zhou, Weidong Yang, and Ying He. 2024. 3D Gaussian as a New Vision Era: A Survey. arXiv preprint arXiv:2402.07181 (2024).
- Laura Fink, Darius Rückert, Linus Franke, Joachim Keinert, and Marc Stamminger. 2023. LiveNVS: Neural View Synthesis on Live RGB-D Streams. (2023).
- Linus Franke, Laura Fink, and Marc Stamminger. 2025. VR-Splatting: Foveated Radiance Field Rendering via 3D Gaussian Splatting and Neural Points. *Proc. ACM Comput. Graph. Interact. Tech.* 8, 1, Article 18 (May 2025). <https://doi.org/10.1145/3728302>
- Linus Franke, Darius Rückert, Laura Fink, Matthias Innmann, and Marc Stamminger. 2023. VET: Visual Error Tomography for Point Cloud Completion and High-Quality Neural Rendering. In *SIGGRAPH Asia 2023 Conference Papers* (Sydney, NSW, Australia) (SA '23). Association for Computing Machinery, New York, NY, USA, Article 38, 12 pages. <https://doi.org/10.1145/3610548.3618212>
- Linus Franke, Darius Rückert, Laura Fink, and Marc Stamminger. 2024. TRIPS: Trilinear Point Splatting for Real-Time Radiance Field Rendering. *Computer Graphics Forum* 43, 2 (2024). <https://doi.org/10.1111/cgf.15102>
- Michael Goesele, Noah Snavely, Brian Curless, Hugues Hoppe, and Steven M. Seitz. 2007. Multi-view stereo for community photo collections. In *2007 IEEE 11th International Conference on Computer Vision*. IEEE, 1–8.
- Florian Hahlbohm, Fabian Friederichs, Tim Weyrich, Linus Franke, Moritz Kappel, Susana Castillo, Marc Stamminger, Martin Eisemann, and Marcus Magnor. 2025. Efficient Perspective-Correct 3D Gaussian Splatting Using Hybrid Transparency. *Computer Graphics Forum* 44, 2 (2025). <https://doi.org/10.1111/cgf.70014>
- Mathias Harrer, Linus Franke, Laura Fink, Marc Stamminger, and Tim Weyrich. 2023. InoVis: Instant Novel-View Synthesis. In *SIGGRAPH Asia Conference Papers* (Sydney, NSW, Australia, December 12–15, 2023). Association for Computing Machinery, New York, NY, USA, 12 pages. <https://doi.org/10.1145/3610548.3618216>
- Mariam Hassan, Florent Forest, Olga Fink, and Malcolm Mielle. 2024. ThermoNeRF: Multimodal Neural Radiance Fields for Thermal Novel View Synthesis. arXiv:2403.12154 [cs.CV]
- Yirui Huang, Zhenhui Ren, Dongming Li, and Xuan Liu. 2020. Phenotypic techniques and applications in fruit trees: a review. *Plant Methods* 16, 1 (2020), 107. <https://doi.org/10.1186/s13007-020-00649-7>
- M. Irani and P. Anandan. 1998. Robust multi-sensor image alignment. In *Sixth International Conference on Computer Vision (IEEE Cat. No.98CH36271)*. 959–966. <https://doi.org/10.1109/ICCV.1998.710832>
- Ray D. Jackson and Alfredo R. Huete. 1991. Interpreting vegetation indices. *Preventive Veterinary Medicine* 11, 3 (1991), 185–200. [https://doi.org/10.1016/S0167-5877\(05\)80004-2](https://doi.org/10.1016/S0167-5877(05)80004-2)
- Bernhard Kerbl, Georgios Kopanas, Thomas Leimkühler, and George Drettakis. 2023. 3D Gaussian Splatting for Real-Time Radiance Field Rendering. *ACM Transactions on Graphics* 42, 4 (July 2023). <https://repo-sam.inria.fr/fungraph/3d-gaussian-splatting/>
- Bernhard Kerbl, Andreas Meuleman, Georgios Kopanas, Michael Wimmer, Alexandre Lanvin, and George Drettakis. 2024. A hierarchical 3d gaussian representation for real-time rendering of very large datasets. *ACM Transactions on Graphics (TOG)* 43, 4 (2024), 1–15.
- Jeffrey P. Kern and Marios S. Pattichis. 2007. Robust Multispectral Image Registration Using Mutual-Information Models. *IEEE Transactions on Geoscience and Remote Sensing* 45, 5 (2007), 1494–1505. <https://doi.org/10.1109/TGRS.2007.892599>
- Shakiba Kheradmand, Daniel Rebain, Gopal Sharma, Weiwei Sun, Yang-Che Tseng, Hossam Isack, Abhishek Kar, Andrea Tagliasacchi, and Kwang Moo Yi. 2024. 3D Gaussian Splatting as Markov Chain Monte Carlo. In *Advances in Neural Information Processing Systems (NeurIPS)*. Spotlight Presentation.
- Georgios Kopanas, Thomas Leimkühler, Gilles Rainer, Clément Jambon, and George Drettakis. 2022. Neural Point Catacaustics for Novel-View Synthesis of Reflections. *ACM TOG* 41, 6 (2022).
- Georgios Kopanas, Julien Philip, Thomas Leimkühler, and George Drettakis. 2021. Point-Based Neural Rendering with Per-View Optimization. *Computer Graphics Forum* (2021). <https://doi.org/10.1111/cgf.14339>
- Jiabao Li, Yuqi Li, Ciliang Sun, Chong Wang, and Jinhui Xiang. 2024a. SPEC-NeRF: Multi-Spectral Neural Radiance Fields. In *ICASSP 2024 - 2024 IEEE International Conference on Acoustics, Speech and Signal Processing (ICASSP)*. 2485–2489. <https://doi.org/10.1109/ICASSP48485.2024.10446015>
- Ru Li, Jia Liu, Guanghui Liu, Shengping Zhang, Bing Zeng, and Shuaicheng Liu. 2024b. SpectralNeRF: physically based spectral rendering with neural radiance field. In *Proceedings of the Thirty-Eighth AAAI Conference on Artificial Intelligence and Thirty-Sixth Conference on Innovative Applications of Artificial Intelligence and Fourteenth Symposium on Educational Advances in Artificial Intelligence (AAAI'24/IAAI'24/EAAI'24)*. AAAI Press, Article 351, 9 pages. <https://doi.org/10.1609/aaai.v38i4.28099>
- Jiaqi Lin, Zhihao Li, Xiao Tang, Jianzhuang Liu, Shiyong Liu, Jiayue Liu, Yangdi Lu, Xiaofei Wu, Songcen Xu, Youliang Yan, and Wenming Yang. 2024a. VastGaussian: Vast 3D Gaussians for Large Scene Reconstruction. In *CVPR*.
- Yvette Y Lin, Xin-Yi Pan, Sara Fridovich-Keil, and Gordon Wetzstein. 2024b. Thermal-NeRF: Thermal Radiance Fields. In *IEEE International Conference on Computational Photography (ICCP)*. IEEE.
- David G Lowe. 1999. Object recognition from local scale-invariant features. In *Proceedings of the seventh IEEE international conference on computer vision*, Vol. 2. IEEE, 1150–1157.
- Rongfeng Lu, Hangyu Chen, Zunjie Zhu, Yuhang Qin, Ming Lu, Le Zhang, Chenggang Yan, and Anke Xue. 2024a. ThermalGaussian: Thermal 3D Gaussian Splatting. arXiv:2409.07200 [cs.CV] <https://arxiv.org/abs/2409.07200>
- Rongfeng Lu, Hangyu Chen, Zunjie Zhu, Yuhang Qin, Ming Lu, Le Zhang, Chenggang Yan, and Anke Xue. 2024b. ThermalGaussian: Thermal 3D Gaussian Splatting. arXiv:2409.07200 [cs.CV] <https://arxiv.org/abs/2409.07200>
- Jonathon Luiten, Georgios Kopanas, Bastian Leibe, and Deva Ramanan. 2024. Dynamic 3D Gaussians: Tracking by Persistent Dynamic View Synthesis. In *3DV*.
- F. Maes, A. Collignon, D. Vandermeulen, G. Marchal, and P. Suetens. 1997. Multimodality image registration by maximization of mutual information. *IEEE Transactions on Medical Imaging* 16, 2 (1997), 187–198. <https://doi.org/10.1109/42.563664>

- T. Berriel Martins and Javier Civera. 2024. Feature Splatting for Better Novel View Synthesis with Low Overlap. arXiv:2405.15518 [cs.CV] <https://arxiv.org/abs/2405.15518>
- Leland McInnes, John Healy, and Steve Astels. 2017. hdbscan: Hierarchical density based clustering. *The Journal of Open Source Software* 2 (03 2017). <https://doi.org/10.21105/joss.00205>
- Lukas Meyer, Andrei-Timotei Ardelean, Tim Weyrich, and Marc Stamminger. 2024a. FruitNeRF++: A Generalized Multi-Fruit Counting Method Utilizing Contrastive Learning and Neural Radiance Fields. *ArXiv* (September 2024). https://meyer.l.githu.io/fruit_nerfpp
- Lukas Meyer, Andreas Gilson, Ute Schmid, and Marc Stamminger. 2024b. FruitNeRF: A Unified Neural Radiance Field based Fruit Counting Framework. https://meyer.l.githu.io/fruit_nerf
- Ben Mildenhall, Pratul P. Srinivasan, Matthew Tancik, Ravi Barron, Jonathan T. and Ramamoorthi, and Ren Ng. 2020. NeRF: Representing Scenes as Neural Radiance Fields for View Synthesis. In *European Conference on Computer Vision*. 405–421.
- Thomas Müller, Alex Evans, Christoph Schied, and Alexander Keller. 2022. Instant neural graphics primitives with a multiresolution hash encoding. *ACM Transactions on Graphics (TOG)* 41, 4, Article 102 (jul 2022), 15 pages.
- Simon Niedermayr, Josef Stumpfegger, and Rüdiger Westermann. 2024. Compressed 3D Gaussian Splatting for Accelerated Novel View Synthesis. In *Proceedings of the IEEE/CVF Conference on Computer Vision and Pattern Recognition (CVPR)*. 10349–10358.
- Michael Niemeyer, Fabian Manhardt, Marie-Julie Rakotosaona, Michael Oechsle, Daniel Duckworth, Rama Gosula, Keisuke Tateno, John Bates, Dominik Kaeser, and Federico Tombari. 2024. Radsplat: Radiance field-informed gaussian splatting for robust real-time rendering with 900+ fps. *arXiv preprint arXiv:2403.13806* (2024).
- Raphael Oefeelin. 2023. *Projektstudie: 3D-Modellierung von Nutzpflanzen mithilfe von Neural Radiance Fields und hyperspektralen Kameraaufnahmen zur Berechnung des Vegetationsindexes*. Technical Report. Hochschule Weihenstephan–Triesdorf, Fakultät Umweltingenieurwesen. https://www.hs-wt.de/fileadmin/Redaktion/Hochschule/Organisation/Zentrale_Einrichtungen/Zentrum_fuer_Forschung_und_Wissenstransfer/Kompetenzzentrum_fuer_Digitale_Agrarwirtschaft/NeRF_Projektstudie_small_final.pdf Projektstudie.
- Tommy Ojo, Thai La, Andrew Morton, and Ian Stavness. 2024. Splanting: 3D plant capture with gaussian splatting (SA '24). Association for Computing Machinery, New York, NY, USA, Article 30, 4 pages. <https://doi.org/10.1145/3681758.3698009>
- M. Özer, Maximilian Weiherer, Martin Hundhausen, and Bernhard Egger. 2024. Exploring Multi-modal Neural Scene Representations With Applications on Thermal Imaging. *ArXiv abs/2403.11865* (2024). <https://api.semanticscholar.org/CorpusID:268531403>
- Matteo Poggi, Pierluigi Zama Ramirez, Fabio Tosi, Samuele Salti, Luigi Di Stefano, and Stefano Mattoccia. 2022. Cross-Spectral Neural Radiance Fields. In *Proceedings of the International Conference on 3D Vision*. 3DV.
- Lukas Radl, Michael Steiner, Mathias Parger, Alexander Weinrauch, Bernhard Kerbl, and Markus Steinberger. 2024. StopThePop: Sorted Gaussian Splatting for View-Consistent Real-time Rendering. *ACM TOG* 4, 43, Article 64 (2024).
- Ruslan Rakhimov, Andrei-Timotei Ardelean, Victor Lempitsky, and Evgeny Burnaev. 2022. NPBG++: Accelerating Neural Point-Based Graphics. In *Proceedings of the IEEE/CVF Conference on Computer Vision and Pattern Recognition (CVPR)*. 15948–15958.
- Darius Rückert, Linus Franke, and Marc Stamminger. 2022. ADOP: approximate differentiable one-pixel point rendering. *ACM Trans. Graph.* 41, 4, Article 99 (July 2022), 14 pages. <https://doi.org/10.1145/3528223.3530122>
- Farah Saeed, Jin Sun, Peggy Ozias-Akins, Ye Juliet Chu, and Changying Charlie Li. 2023. PeanutNeRF: 3D Radiance Field for Peanuts. In *2023 IEEE/CVF Conference on Computer Vision and Pattern Recognition Workshops (CVPRW)*. 6254–6263. <https://doi.org/10.1109/CVPRW59228.2023.00665>
- Johannes Lutz Schönberger and Jan-Michael Frahm. 2016. Structure-from-motion revisited. In *Proceedings of the IEEE conference on computer vision and pattern recognition*. 4104–4113.
- Johannes L. Schönberger and Jan-Michael Frahm. 2016. Structure-from-Motion Revisited. *CVPR* (2016).
- Johannes Lutz Schönberger, Enliang Zheng, Marc Pollefeys, and Jan-Michael Frahm. 2016. Pixelwise View Selection for Unstructured Multi-View Stereo. In *European Conference on Computer Vision (ECCV)*. Springer International Publishing, Cham.
- Harry Shum and Sing Bing Kang. 2000. Review of image-based rendering techniques. In *Visual Communications and Image Processing 2000*, Vol. 4067. SPIE, 2–13.
- Heung-Yeung Shum, Shing-Chow Chan, and Sing Bing Kang. 2008. *Image-based rendering*. Springer Science & Business Media.
- Saptarshi Neil Sinha, Holger Graf, and Michael Weinmann. 2024. SpectralGaussians: Semantic, spectral 3D Gaussian splatting for multi-spectral scene representation, visualization and analysis. arXiv:2408.06975 [cs.CV] <https://arxiv.org/abs/2408.06975>
- Claus Smitt, Michael Halstead, Patrick Zimmer, Thomas Läbe, Esra Guclu, Cyrill Stachniss, and Chris McCool. 2023. PAg-NeRF: Towards fast and efficient end-to-end panoptic 3D representations for agricultural robotics. arXiv:2309.05339 [cs.RO] <https://arxiv.org/abs/2309.05339>
- Noah Snavely, Steven M. Seitz, and Richard Szeliski. 2006. Photo tourism: exploring photo collections in 3D. Vol. 25. Association for Computing Machinery, New York, NY, USA, 835–846.
- Matthew Tancik, Ethan Weber, Evonne Ng, Ruilong Li, Brent Yi, Terrance Wang, Alexander Kristoffersen, Jake Austin, Kamyar Salahi, Abhik Ahuja, David McAllister, Justin Kerr, and Angjoo Kanazawa. 2023. Nerfstudio: A Modular Framework for Neural Radiance Field Development. In *ACM SIGGRAPH 2023 Conference Proceedings* (Los Angeles, CA, USA) (*SIGGRAPH '23*). Association for Computing Machinery, New York, NY, USA, Article 72, 12 pages. <https://doi.org/10.1145/3588432.3591516>
- Ayush Tewari, Ohad Fried, Justus Thies, Vincent Sitzmann, Stephen Lombardi, Kalyan Sunkavalli, Ricardo Martin-Brualla, Tomas Simon, Jason Saragih, Matthias Nießner, Rohit Pandey, Sean Fanello, Gordon Wetzstein, Jun-Yan Zhu, Christian Theobalt, Maneesh Agrawala, Eli Shechtman, Dan B. Goldman, and Michael Zollhöfer. 2020. State of the Art on Neural Rendering. *Computer Graphics Forum* 39, 2, 701–727.
- Ayush Tewari, Justus Thies, Ben Mildenhall, Pratul Srinivasan, Edgar Treitsch, Yifan Wang, Christoph Lassner, Vincent Sitzmann, Ricardo Martin-Brualla, Stephen Lombardi, Tomas Simon, Christian Theobalt, Matthias Niessner, Jonathan T. Barron, Gordon Wetzstein, Michael Zollhoefer, and Vladislav Golyanik. 2022. Advances in Neural Rendering. *Computer Graphics Forum* 41, 2, 703–735.
- Christopher Thirgood, Oscar Mendez, Erin Ling, Jon Storey, and Simon Hadfield. 2024. HyperGS: Hyperspectral 3D Gaussian Splatting. <https://doi.org/10.48550/arXiv.2412.12849>
- Oleg Voynov, Gleb Bobrovskikh, Pavel Karpyshev, Saveliy Galochkin, Andrei-Timotei Ardelean, Arseniy Bozhcnko, Ekaterina Karmanova, Pavel Kopanov, Yaroslav Labutin-Rymsho, Ruslan Rakhimov, Aleksandr Safin, Valerii Serpiva, Alexey Artemov, Evgeny Burnaev, Dzhmityr Tsetserukou, and Denis Zorin. 2023. Multi-Sensor Large-Scale Dataset for Multi-View 3D Reconstruction. In *2023 IEEE/CVF Conference on Computer Vision and Pattern Recognition (CVPR)*. 21392–21403. <https://doi.org/10.1109/CVPR52729.2023.02049>
- A. N. Wilson, Khushi Anil Gupta, Balu Harshavardan Koduru, Abhinav Kumar, Ajit Jha, and Linga Reddy Cenkeramaddi. 2023. Recent Advances in Thermal Imaging and its Applications Using Machine Learning: A Review. *IEEE Sensors Journal* 23, 4 (2023), 3395–3407. <https://doi.org/10.1109/JSEN.2023.3234335>
- Guanjun Wu, Taoran Yi, Jiemin Fang, Lingxi Xie, Xiaopeng Zhang, Wei Wei, Wenyu Liu, Qi Tian, and Xinggang Wang. 2024a. 4d gaussian splatting for real-time dynamic scene rendering. In *Proceedings of the IEEE/CVF Conference on Computer Vision and Pattern Recognition*. 20310–20320.
- Tong Wu, Yu-Jie Yuan, Ling-Xiao Zhang, Jie Yang, Yan-Pei Cao, Ling-Qi Yan, and Lin Gao. 2024b. Recent advances in 3d gaussian splatting. *Computational Visual Media* 10, 4 (2024), 613–642.
- Jiacong Xu, Mingqian Liao, Ram Prabhakar Kathirvel, and Vishal M. Patel. 2025. Leveraging Thermal Modality to Enhance Reconstruction in Low-Light Conditions. In *Computer Vision – ECCV 2024*, Aleš Leonardis, Elisa Ricci, Stefan Roth, Olga Russakovsky, Torsten Sattler, and Gül Varol (Eds.). Springer Nature Switzerland, Cham.
- Xin Yang, Xuqi Lu, Pengyao Xie, Guo Ziyue, Hui Fang, Haowei Fu, Xiaochun Hu, Zhenbiao Sun, and Haiyan Cen. 2024. PanicleNeRF: Low-Cost, High-Precision In-Field Phenotyping of Rice Panicles with Smartphone. *Plant Phenomics* 6 (12 2024). <https://doi.org/10.34133/plantphenomics.0279>
- Tianxiang Ye, Qi Wu, Junyuan Deng, Guoqing Liu, Liu Liu, Songpengcheng Xia, Liang Pang, Wenxian Yu, and Ling Pei. 2024b. Thermal-NeRF: Neural Radiance Fields from an Infrared Camera. arXiv:2403.10340 [cs.CV] <https://arxiv.org/abs/2403.10340>
- Vickie Ye, Ruilong Li, Justin Kerr, Matias Turkulainen, Brent Yi, Zhuoyang Pan, Otto Seiskari, Jianbo Ye, Jeffrey Hu, Matthew Tancik, and Angjoo Kanazawa. 2025. gsplat: An open-source library for Gaussian splatting. *Journal of Machine Learning Research* 26, 34 (2025), 1–17.
- Zongxin Ye, Wenyu Li, Sidun Liu, Peng Qiao, and Yong Dou. 2024a. AbsGS: Recovering Fine Details for 3D Gaussian Splatting. arXiv:2404.10484 [cs.CV]
- Zehao Yu, Anpei Chen, Binbin Huang, Torsten Sattler, and Andreas Geiger. 2024. Mip-splatting: Alias-free 3d gaussian splatting. In *Proceedings of the IEEE/CVF Conference on Computer Vision and Pattern Recognition*. 19447–19456.
- Kai Zhang, Gernot Riegler, Noah Snavely, and Vladlen Koltun. 2020. Nerf++: Analyzing and improving neural radiance fields. *arXiv preprint arXiv:2010.07492* (2020).
- Xiajun Zheng, Xinyi Ai, Hao Qin, Jiacheng Rong, Zhiqin Zhang, Yan Yang, Ting Yuan, and Wei Li. 2024. Tomato-Nerf: Advancing Tomato Model Reconstruction With Improved Neural Radiance Fields. *IEEE Access* 12 (2024), 184206–184215. <https://doi.org/10.1109/ACCESS.2024.3424908>
- Barbara Zitová and Jan Flusser. 2003. Image registration methods: a survey. *Image and Vision Computing* 21, 11 (2003), 977–1000. [https://doi.org/10.1016/S0262-8856\(03\)00137-9](https://doi.org/10.1016/S0262-8856(03)00137-9)

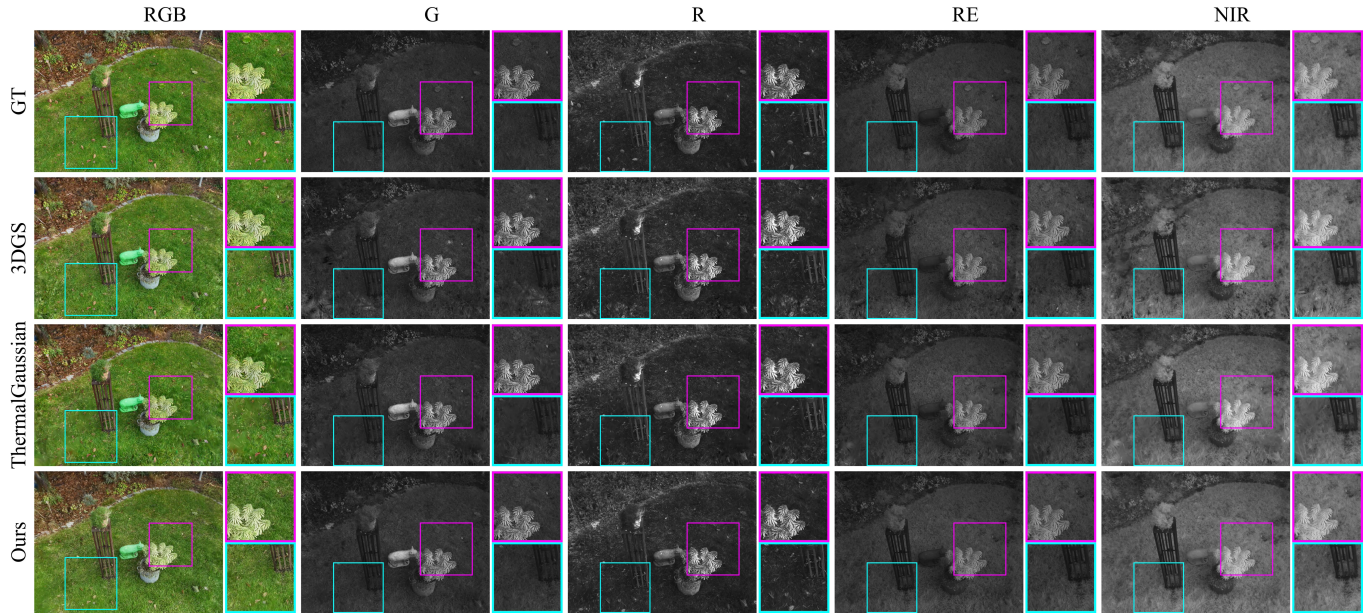


Fig. 6. Visual comparison on the GARDEN scene with all available spectral-bands. The used ThermalGaussian method in this comparison is our multi-spectral re-implementation.

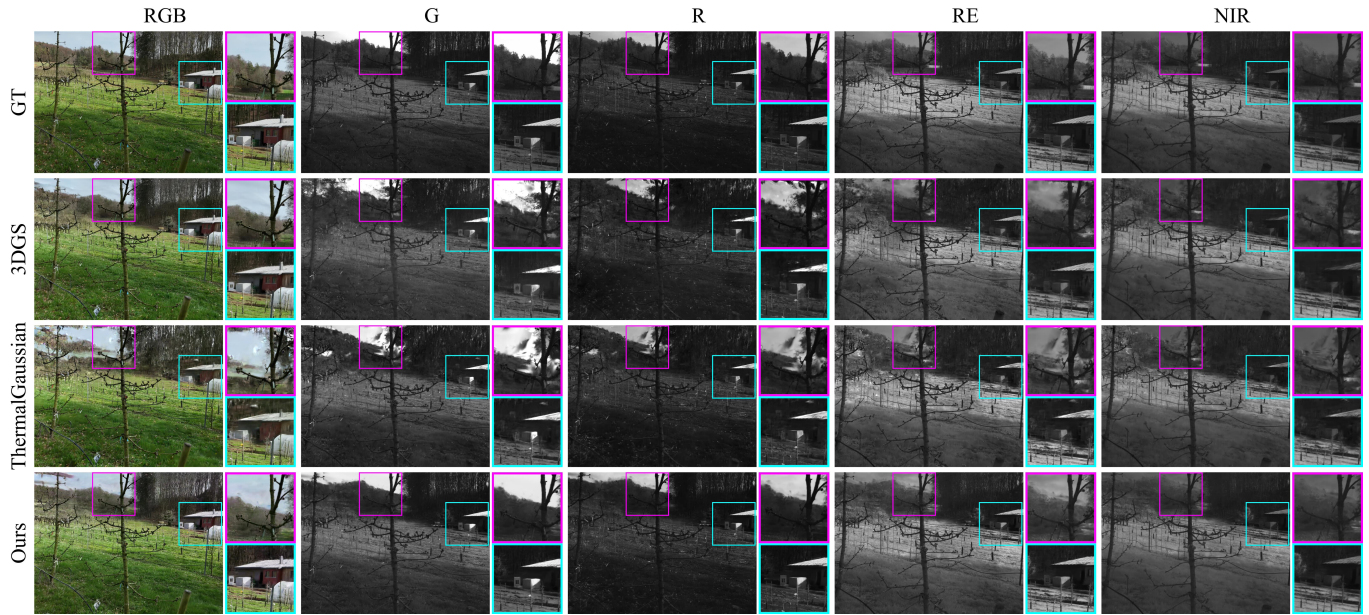


Fig. 7. Visual comparison on the SINGLE TREE scene with all available spectral-bands. The used ThermalGaussian method in this comparison is our multi-spectral re-implementation.

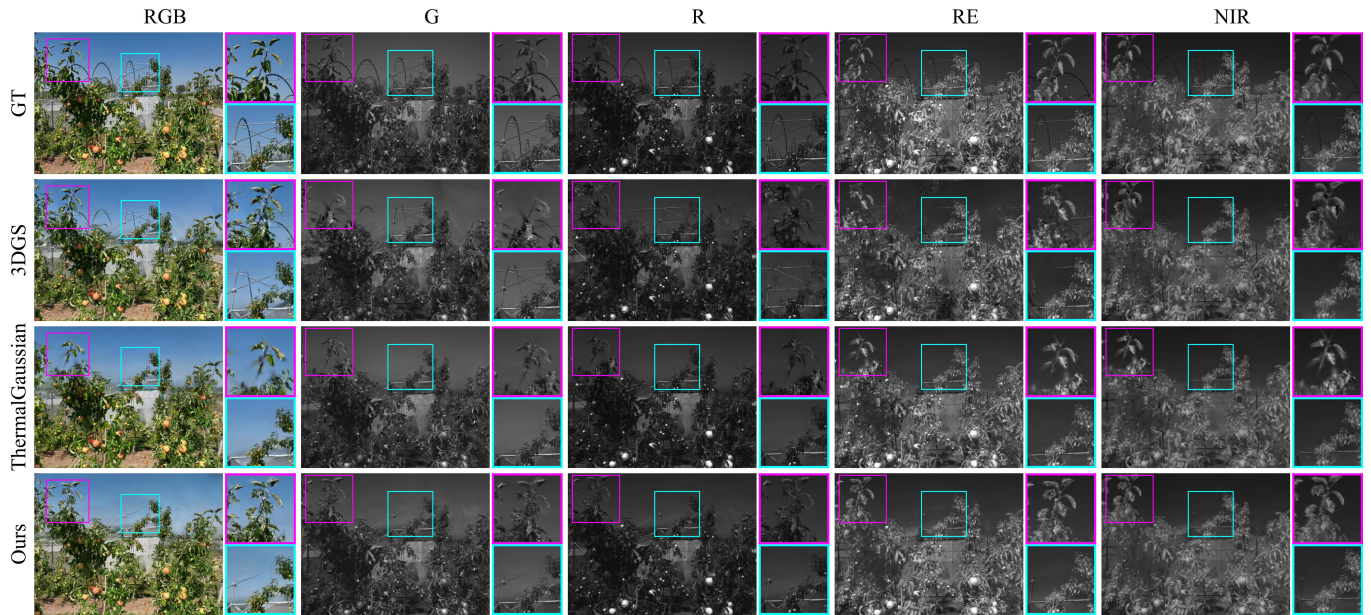


Fig. 8. Visual comparison on the FRUIT TREES scene with all available spectral-bands. The used ThermalGaussian method in this comparison is our multi-spectral re-implementation.

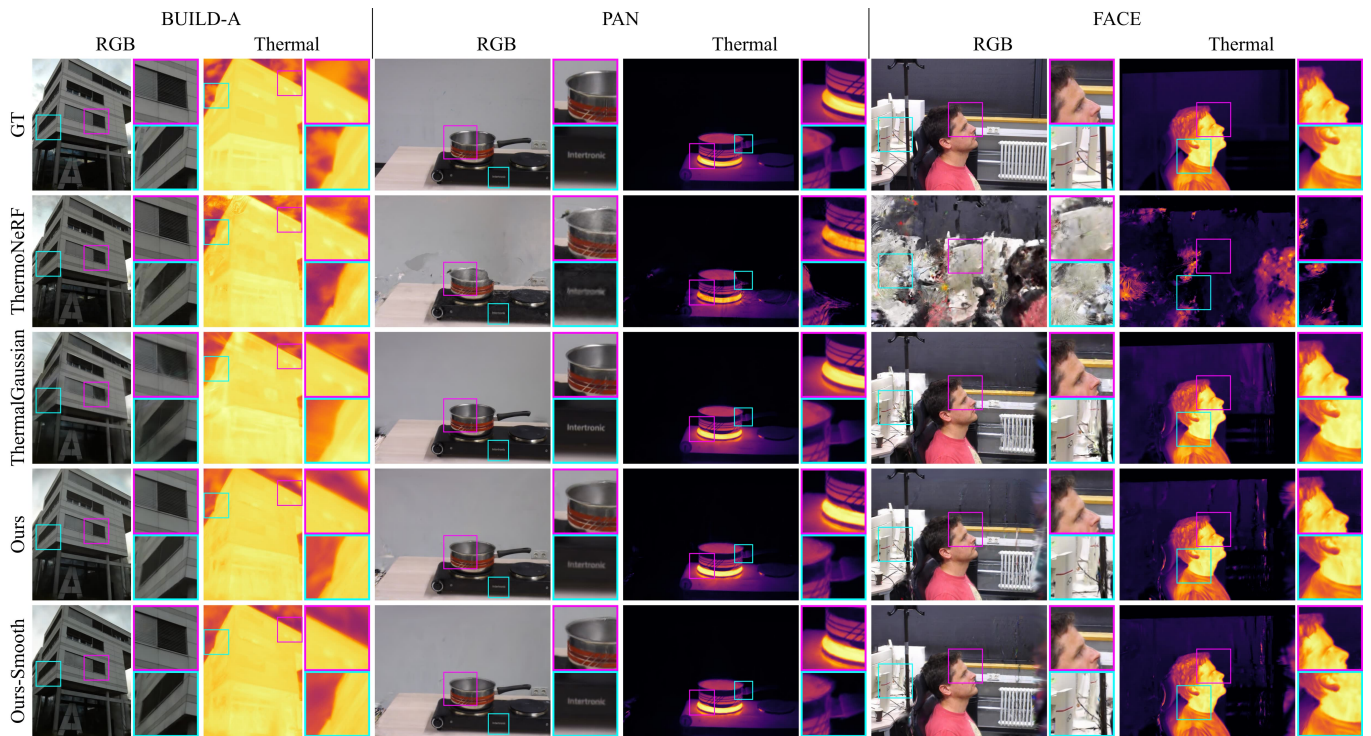


Fig. 9. Visual comparison of the thermal scenes BUILD-A, PAN and FACE on ThermalGaussian, ThermoNeRF and ours. The used ThermalGaussian method is the original implementation by [Lu et al. 2024a]. Ours-Smooth uses the smoothness loss proposed by [Lu et al. 2024a].

SUPPLEMENTAL MATERIAL

In this supplementary material, we provide extra ablation studies and details on experiments and implementation

S1 ABLATION ON MS-SPLATTING

We extended the ablation studies described in Sec.4.4 by an extensive evaluation on the feature normalization (Sec. S1.1), the network size (Sec. S1.2) and the positional encoding (Sec. S1.3). Additionally we provide the full tables of all channels in Tab. S.T6, Tab. S.T7, Tab. S.T8, Tab. S.T9 .

S1.1 Feature Normalization

We also evaluated the impact of the feature normalization on our neural color representation. In Tab. S.T1 both runs with and without normalization are shown. This leads to only a minor improvement on the PSNR. Besides this we sometimes encountered numerical instability with no feature normalization.

Table S.T1. Evaluation of feature normalization. NoNorm has feature normalization deactivated

# Features	PSNR (\uparrow)	SSIM (\uparrow)	LPIPS (\downarrow)
NoNorm	24.80	0.748	0.310
Norm	25.02	0.748	0.310

S1.2 Network Size

To assess the impact of network capacity, we evaluated our pipeline using MLPs of various sizes. Specifically, we varied the number of hidden layers (0, 1, or 2) and the width of each layer (from 16 to 128 neurons). Tab. S.T2 summarizes the results, averaged over all datasets. Overall, a single hidden layer yields the best trade-off across configurations. Extremely shallow networks (no hidden layers) or very deep, wide networks (two layers of width 128) struggle to learn accurate color representations, resulting in washed-out and dull renderings.

Table S.T2. Impact of MLP size on rendering quality. The network uses a feature encoding of dimension 16 as input. Results are averaged over all datasets. $[L \times W]$ denotes [Layer Depth \times Layer Width].

Hidden Size	PSNR (\uparrow)	SSIM (\uparrow)	LPIPS (\downarrow)
$L = 0, W = 16$	24.89	0.747	0.312
$L = 0, W = 32$	24.91	0.746	0.314
$L = 0, W = 64$	24.96	0.747	0.312
$L = 0, W = 128$	24.97	0.747	0.311
$L = 1, W = 16$	24.59	0.742	0.317
$L = 1, W = 32$	25.02	0.748	0.310
$L = 1, W = 64$	25.03	0.748	0.311
$L = 1, W = 128$	25.04	0.749	0.310
$L = 2, W = 16$	24.97	0.747	0.312
$L = 2, W = 32$	24.74	0.746	0.314
$L = 2, W = 64$	24.81	0.746	0.315
$L = 2, W = 128$	23.85	0.721	0.373

Table S.T3. Comparison of positional encoding on the viewing direction (DE) and the splat position (PE).

Encoding	PSNR (\uparrow)	SSIM (\uparrow)	LPIPS (\downarrow)
None	25.02	0.748	0.310
PE[0]	24.48	0.739	0.326
PE[5]	24.62	0.743	0.320
PE[10]	24.57	0.743	0.322
DE[0]	25.29	0.754	0.304
DE[5]	25.23	0.746	0.313
DE[10]	25.29	0.745	0.315
PE[0]-DE[0]	25.09	0.753	0.307
PE[5]-DE[5]	25.12	0.747	0.314
PE[10]-DE[10]	25.17	0.746	0.316

S1.3 Positional Encoding

FeatSplat [Martins and Civera 2024] proposed to input the viewing direction as an additional parameter to the MLP. Here, we tried whether the *normalized* viewing direction or the normalized splat position can improve the results. Additionally, we tested positional encoding on both arguments with 0, 5, and 10 frequencies. In the case of 0, only the viewing direction with no encoding is meant. The results are shown in Tab. S.T3. It is clearly visible that positional encoding on the viewing direction improves the result, while the positional encoding on the splats position degrades the evaluation results. From a rendering perspective, adding the viewing direction to the MLP seems to be similar to the view-dependent representation of spherical harmonics.

Table S.T4. Comparison of the approaches ThermoNeRF, ThermalGaussian and our approach on six thermal scenes, combining RGB and thermal (T) images. Three scenes are from ThermalNeRF [Özer et al. 2024] (FACE, LION, PAN) and three scenes from ThermoNeRF [Hassan et al. 2024] (BUILD-A (buildingA_spring), ROBOT (double_robot), KETTLE (heater_water_kettle))

Dataset	Metric	PSNR (\uparrow)		SSIM (\uparrow)		LPIPS (\downarrow)	
		RGB	T	RGB	T	RGB	T
FACE	Thermal Gaus.	22.05	27.65	0.816	0.824	0.187	0.217
	ThermoNeRF	9.76	10.43	0.254	0.395	0.712	0.657
	Ours	26.74	28.73	0.904	0.874	0.132	0.235
	Ours + \mathcal{L}_{smooth}	24.62	26.50	0.884	0.864	0.148	0.228
LION	Thermal Gaus.	31.42	30.21	0.936	0.934	0.121	0.122
	ThermoNeRF	20.12	23.88	0.723	0.735	0.180	0.422
	Ours	29.21	28.30	0.923	0.913	0.140	0.150
	Ours + \mathcal{L}_{smooth}	31.41	29.90	0.948	0.931	0.115	0.141
PAN	Thermal Gaus.	29.23	36.03	0.932	0.939	0.123	0.028
	ThermoNeRF	15.96	22.75	0.608	0.774	0.353	0.136
	Ours	29.75	34.59	0.946	0.929	0.106	0.052
	Ours + \mathcal{L}_{smooth}	29.65	35.30	0.945	0.930	0.107	0.050
BUILD-A	Thermal Gaus.	22.70	28.79	0.812	0.975	0.253	0.121
	ThermoNeRF	19.74	26.27	0.635	0.931	0.250	0.185
	Ours	23.24	28.60	0.838	0.973	0.193	0.098
	Ours + \mathcal{L}_{smooth}	24.89	28.85	0.877	0.976	0.157	0.077
ROBOT	Thermal Gaus.	19.90	30.62	0.727	0.944	0.353	0.118
	ThermoNeRF	17.35	27.56	0.615	0.888	0.300	0.151
	Ours	22.64	33.00	0.836	0.959	0.237	0.059
	Ours + \mathcal{L}_{smooth}	23.15	33.13	0.845	0.959	0.226	0.046
KETTLE	Thermal Gaus.	24.15	34.73	0.719	0.968	0.319	0.035
	ThermoNeRF	16.30	23.83	0.438	0.865	0.458	0.221
	Ours	26.27	33.89	0.848	0.955	0.187	0.030
	Ours + \mathcal{L}_{smooth}	26.24	33.72	0.850	0.950	0.187	0.031

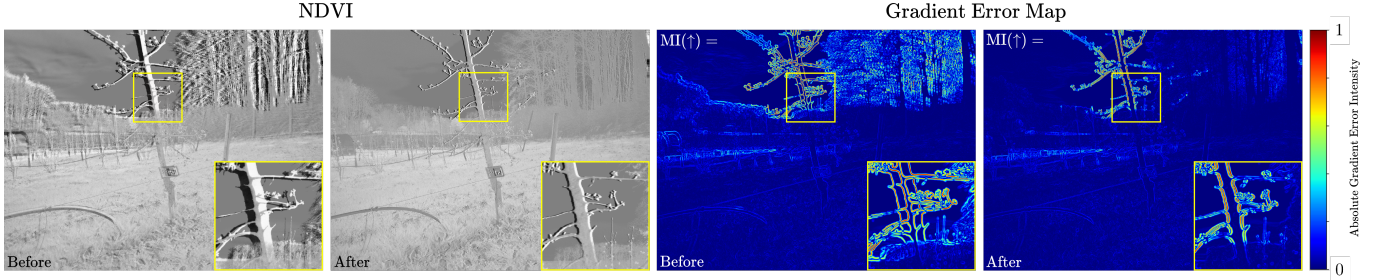


Fig. S.F1. Image registration based on mutual information (MI). The top row visualizes an overlay of the near-infra red (NIR) and red edge (RE) channel with (right) and without registration (left). The bottom row shows the edge-based error map with (right) and without registration (left). The registration reduces the visual artifacts but artifacts at the top of the tree still remain.

S2 MULTI-MODAL EVALUATION

We evaluated each scene using the original ThermalGaussian [Lu et al. 2024a], ThermoNeRF [Hassan et al. 2024], and our implementation. We additionally added the smoothness loss from ThermalGaussian. It encourages spatial smoothness, and is defined through:

$$\mathcal{L}_{\text{smooth}} = \frac{1}{4M} \sum_{i,j} (|T_{i\pm 1,j} - T_{i,j}| + |T_{i,j\pm 1} - T_{i,j}|). \quad (8)$$

where $T_{i,j}$ denotes the rendered thermal pixel at image coordinates (i, j) , and M is the total number of rendered pixels. While RGB images often exhibit sharp changes at object boundaries, thermal images typically vary smoothly in a local neighborhood. Therefore, this loss yields smoother thermal reconstructions.

We trained ThermalGaussian [Lu et al. 2024a] and ThermoNeRF [Hassan et al. 2024] for 30,000 iterations, whereas our model was trained for 60,000 iterations. We set the feature dimension to $d = 8$, and use a single hidden layer with 32 neurons. In addition, we concatenate the viewing direction \mathbf{d} to the feature embedding f . We adapt our multi-spectral Gaussian strategy, as we first train on RGB only for 5,000 iterations, then continue with joint RGB-thermal optimization. This allows the Gaussian model to learn coarse geometry from RGB before incorporating the less spatially detailed thermal modality. See Tab. S.T4 for quantitative results and Fig. 9 for a visual comparison.

S3 MULTI-SPECTRAL IMAGE REGISTRATION FOR VEGETATION INDICES

As a baseline for our novel view synthesis vegetation index computation we need a method to estimate a transformation T to map our target image A to a reference image B . Therefore we utilize an image registration method which is based on mutual information (MI). This method is mainly used for the registration of multi-modal data such as computed tomography and magnetic resonance data [Kern and Pattichis 2007; Maes et al. 1997; Zitová and Flusser 2003]. The concept states that MI is maximized if two images are geometrically aligned and thus makes no assumption regarding the intensity relations between multi-modal data. This is beneficial for multi-spectral channels such as NIR as it has significant less textural information such as red and green channels.

Mutual information [Maes et al. 1997] measures the degree of dependence between A and B by measuring the similarity between the joint probability distribution $p(a, b)$ and the product of the marginal distributions $p(a), p(b)$. In the case of complete independence MI converges towards 0 and for dependent distributions MI maximizes with increasing similarity between $p(a)$ and $p(b)$. MI is defined by

$$I(A; B) = \sum_{a \in A} \sum_{b \in B} p(a, b) \log \left(\frac{p(a, b)}{p(a)p(b)} \right), \quad (9)$$

whereas A and B are random variables, $p(a, b)$ is defined as the joint probability distribution and $p(a), p(b)$ are the marginal distributions. If we consider a and b to be the images intensity values of corresponding pixel pairs in both images we can estimate the joint and marginal distributions by obtaining the joint and marginal histograms of the image pair [Maes et al. 1997].

By maximizing the mutual information through the application of a rigid transformation $T(\mathbf{x}) = R\mathbf{x} + \mathbf{t}$ on the target image B we can determine a feasible set of registration parameters through,

$$T^* = \underset{T}{\operatorname{argmax}} I(A; T \circ B). \quad (10)$$

By using Powell’s multidimensional method to maximize the mutual information $I(A; B)$ and defining a limited search space for the translation t_x and t_y and the rotation ϕ we can find a feasible transformation matrix to align our multi-spectral data.

In Fig. S.F1 we demonstrate on the left the computation of the NDVI without and with MI image registration. To quantify the structural discrepancies between two images, we compute a gradient-based error map by measuring the absolute differences between their gradient magnitudes (Sobel), which is visualized on the right in Fig. S.F1.

A result of an image registration of a NIR and red channel image is depicted in Fig. S.F1. In the top row an overlay of both images are visualized before and after registration. On the left image the blurry artifacts are visible and on the right a reduced intensity of errors is visible. This is also shown in the bottom row of Fig. S.F1. It visualizes the edge/gradient error map of the registered images and emphasizes the error minimization due to the registration process. Despite image registration, the error remains present, albeit less significant.

Table S.T5. Comparison between original ThermalGaussian (TG) on our warped dataset (W), our re-implementation (TG-Ours) on the warped dataset, and our re-implementation on the original dataset (O). Averaged across all 7 scenes.

	PSNR (\uparrow)						SSIM (\uparrow)						LPIPS (\downarrow)					
	All	RGB	G	R	RE	NIR	All	RGB	G	R	RE	NIR	All	RGB	G	R	RE	NIR
TG (W)	23.54	19.81	23.98	25.66	23.78	24.49	0.700	0.565	0.710	0.763	0.717	0.743	0.342	0.371	0.336	0.305	0.336	0.362
TG-Ours (W)	23.14	18.81	23.83	25.27	23.38	24.42	0.676	0.482	0.697	0.752	0.701	0.749	0.378	0.483	0.367	0.331	0.357	0.355
TG-Ours (O)	25.65	21.17	25.42	27.79	25.79	28.13	0.763	0.633	0.729	0.827	0.780	0.849	0.266	0.306	0.293	0.240	0.257	0.232

S4 THERMAL GAUSSIAN RE-IMPLEMENTATION

To allow for proper comparison of methods on our datasets, we adapted the OMMG (One Multi-Modal Gaussian) approach introduced by ThermalGaussian [Lu et al. 2024a] for multi-spectral view-independent input data. For this, analog to their method, we model each Gaussian as containing separate spherical harmonics (SH) coefficients for every spectral band, e.g. RGB, MS-G, MS-R, MS-RE and NIR.

To allow for independent camera poses across the multi-spectral dataset, during each training iteration, we select a single image from a given spectral band, and optimize only the SH coefficients corresponding to that band. This is different to the method of [Lu et al. 2024a], since they render and optimize both the RGB and thermal channel in a single forward pass. Optimization of Gaussian positions, scales, rotations and opacities is unchanged and performed during all iterations. Standard Gaussian densification, as described by [Kerbl et al. 2023], is performed every 100 iterations.

Tab. S.T5 compares our re-implementation (TG-Ours) with the original ThermalGaussian implementation (TG). For TG, we utilized the warped version of our dataset and trained in four separate runs, each selecting the RGB images combined with one multi-spectral band, trained for 30,000 iterations. TG-Ours ran on the combined set of all 5 channels in a single model, once with warped images, and once with the original data. Since our approach splits the training of different bands into consecutive iterations, we chose 120,000 iterations. In the average over all 7 scenes, we observe that our re-implementation performs slightly worse than the original ThermalGaussian on warped datasets. However, TG-ours can leverage multi-spectral images with independent camera positions, which avoids errors introduced by image warping. We observe that TG-Ours on the original images consistently outperforms original ThermalGaussian. For this reason, we conclude that our re-implementation appropriately represents the method utilized by [Lu et al. 2024a] and we use it in the evaluation of our method.

Table S.T6. Evaluation on our densification strategy with all spectral bands. Densification interval with *Default* and *MaxAverage* (Ours) Strategy. 3DGS default is listed as *Default - 100*. The colors indicate the **best** and **worst** results.

	PSNR (\uparrow)						SSIM (\uparrow)						LPIPS (\downarrow)					
	All	RGB	G	R	RE	NIR	All	RGB	G	R	RE	NIR	All	RGB	G	R	RE	NIR
Ours - 500	24.85	20.59	24.61	26.99	24.94	27.20	0.756	0.617	0.723	0.820	0.774	0.846	0.281	0.319	0.309	0.258	0.271	0.247
<i>Default - 500</i>	24.86	20.55	24.65	26.83	24.97	27.35	0.747	0.596	0.717	0.814	0.767	0.843	0.323	0.368	0.353	0.295	0.315	0.282
Ours - 100	24.93	20.57	24.75	27.17	24.97	27.24	0.750	0.613	0.716	0.816	0.767	0.839	0.267	0.305	0.292	0.244	0.260	0.235
Ours - 400	24.93	20.71	24.70	26.96	24.97	27.36	0.749	0.599	0.718	0.816	0.768	0.844	0.320	0.365	0.350	0.293	0.313	0.280
<i>Default - 100</i>	25.02	20.67	24.83	27.10	25.12	27.43	0.748	0.600	0.717	0.815	0.767	0.841	0.310	0.351	0.340	0.283	0.304	0.272
Ours - 200	25.02	20.73	24.82	27.12	25.12	27.38	0.748	0.599	0.717	0.815	0.767	0.841	0.317	0.360	0.346	0.289	0.310	0.278
Ours - 200	25.08	20.85	24.87	27.22	25.07	27.46	0.754	0.618	0.720	0.819	0.771	0.842	0.271	0.307	0.298	0.249	0.263	0.238
<i>Default - 300</i>	25.08	20.67	24.95	27.23	25.18	27.44	0.748	0.599	0.718	0.815	0.768	0.843	0.319	0.363	0.349	0.291	0.311	0.279
Ours - 400	25.09	20.78	24.91	27.21	25.09	27.52	0.757	0.620	0.723	0.822	0.775	0.846	0.275	0.314	0.303	0.252	0.267	0.241
Ours - 300	25.16	20.91	24.97	27.38	25.19	27.40	0.758	0.623	0.723	0.822	0.775	0.845	0.271	0.308	0.298	0.248	0.262	0.237

Table S.T7. Comparison of variation in the neural feature embedding dimension d . Additionally to the main thesis we evaluated a deep MLP of four hidden layers ($D = 4$) and 32 neurons per layer ($W = 32$). The shallow MLP has a one hidden layer ($D=1$) and 32 neurons per layer ($L=32$). For the deep and shallow network, feature normalization is activated by default. Thus for the shallow MLP we deactivate feature normalization (NoNorm). The colors indicate the **best** and **worst** results.

	PSNR (\uparrow)						SSIM (\uparrow)						LPIPS (\downarrow)					
	All	RGB	G	R	RE	NIR	All	RGB	G	R	RE	NIR	All	RGB	G	R	RE	NIR
d = 2-NoNorm	24.74	20.42	24.62	26.71	24.92	27.10	0.743	0.594	0.712	0.809	0.765	0.837	0.320	0.371	0.349	0.290	0.309	0.278
d = 4-NoNorm	24.66	20.47	24.54	26.84	24.66	26.86	0.746	0.598	0.716	0.813	0.766	0.840	0.313	0.358	0.341	0.284	0.305	0.274
d = 8-NoNorm	24.98	20.73	24.79	27.14	24.98	27.31	0.749	0.603	0.718	0.816	0.768	0.842	0.308	0.349	0.338	0.281	0.300	0.270
d = 16-NoNorm	24.80	20.61	24.65	26.94	24.84	27.02	0.748	0.601	0.717	0.814	0.767	0.840	0.310	0.349	0.340	0.284	0.303	0.273
d = 32-NoNorm	24.95	20.69	24.76	27.08	24.97	27.27	0.748	0.602	0.717	0.815	0.768	0.842	0.310	0.351	0.340	0.284	0.304	0.272
d = 64-NoNorm	24.56	20.43	24.34	26.75	24.55	26.76	0.742	0.592	0.710	0.809	0.761	0.837	0.323	0.364	0.354	0.297	0.315	0.283
d = 2-Deep	24.40	20.11	24.31	26.48	24.50	26.66	0.738	0.585	0.708	0.806	0.760	0.835	0.333	0.385	0.361	0.304	0.323	0.292
d = 4-Deep	24.59	20.45	24.48	26.71	24.60	26.77	0.744	0.594	0.714	0.810	0.765	0.837	0.320	0.368	0.349	0.292	0.311	0.280
d = 8-Deep	24.63	20.49	24.58	26.84	24.61	26.70	0.745	0.596	0.716	0.812	0.764	0.837	0.320	0.366	0.348	0.291	0.312	0.282
d = 16-Deep	24.63	20.33	24.54	26.73	24.70	26.92	0.744	0.594	0.714	0.809	0.765	0.839	0.319	0.366	0.347	0.292	0.310	0.278
d = 32-Deep	24.41	20.26	24.38	26.53	24.42	26.51	0.741	0.588	0.712	0.807	0.761	0.836	0.328	0.374	0.356	0.300	0.320	0.288
d = 64-Deep	24.70	20.41	24.61	26.79	24.80	26.93	0.743	0.593	0.713	0.811	0.763	0.835	0.322	0.368	0.351	0.294	0.313	0.282
d = 2	24.50	20.11	24.47	26.59	24.67	26.70	0.739	0.585	0.709	0.806	0.761	0.835	0.329	0.384	0.357	0.302	0.317	0.286
d = 3	24.93	20.54	24.81	27.14	25.05	27.17	0.745	0.596	0.714	0.812	0.767	0.838	0.319	0.367	0.349	0.290	0.309	0.278
d = 4	24.55	20.39	24.45	26.67	24.56	26.74	0.744	0.593	0.714	0.811	0.764	0.838	0.317	0.364	0.346	0.290	0.308	0.277
d = 5	24.56	20.34	24.51	26.70	24.52	26.76	0.742	0.593	0.712	0.809	0.761	0.836	0.319	0.364	0.347	0.293	0.312	0.281
d = 6	24.85	20.64	24.68	27.05	24.86	27.06	0.747	0.600	0.716	0.814	0.765	0.840	0.312	0.356	0.341	0.284	0.305	0.274
d = 7	24.73	20.49	24.57	26.85	24.76	27.02	0.745	0.600	0.715	0.812	0.764	0.839	0.314	0.357	0.342	0.287	0.307	0.275
d = 8	25.06	20.75	24.88	27.14	25.11	27.51	0.749	0.602	0.718	0.815	0.768	0.842	0.308	0.349	0.338	0.282	0.301	0.270
d = 16	25.02	20.67	24.83	27.10	25.12	27.43	0.748	0.600	0.717	0.815	0.767	0.841	0.310	0.351	0.340	0.283	0.304	0.272
d = 32	24.92	20.59	24.77	27.09	24.97	27.22	0.747	0.599	0.718	0.814	0.767	0.840	0.311	0.353	0.340	0.283	0.303	0.273
d = 64	24.85	20.54	24.67	26.98	24.91	27.18	0.747	0.598	0.718	0.814	0.767	0.841	0.311	0.355	0.341	0.284	0.304	0.272

Table S.T8. Variation on the spectral feature decoding network. We sweep over different layer depths L and layer widths W . The colors indicate the **best** and **worst** results.

	PSNR (\uparrow)						SSIM (\uparrow)						LPIPS (\downarrow)					
	All	RGB	G	R	RE	NIR	All	RGB	G	R	RE	NIR	All	RGB	G	R	RE	NIR
$L = 2, W = 256$	16.25	12.79	16.38	18.14	15.73	18.26	0.480	0.313	0.446	0.497	0.519	0.627	0.689	0.798	0.725	0.651	0.669	0.600
$L = 2, W = 192$	20.17	15.80	20.58	22.58	20.54	21.36	0.611	0.443	0.591	0.694	0.627	0.700	0.502	0.582	0.520	0.461	0.496	0.454
$L = 2, W = 128$	23.85	19.82	23.95	25.96	23.99	25.54	0.721	0.558	0.697	0.792	0.744	0.816	0.373	0.435	0.396	0.337	0.362	0.332
$L = 1, W = 256$	24.34	20.33	24.28	26.40	24.45	26.27	0.732	0.581	0.706	0.801	0.752	0.824	0.351	0.405	0.371	0.318	0.344	0.316
$L = 1, W = 16$	24.59	20.29	24.33	26.66	24.70	27.02	0.742	0.593	0.711	0.808	0.763	0.838	0.317	0.361	0.345	0.290	0.309	0.277
$L = 1, W = 192$	24.72	20.41	24.63	26.88	24.68	27.04	0.743	0.594	0.714	0.809	0.762	0.837	0.325	0.371	0.351	0.296	0.319	0.288
$L = 2, W = 32$	24.74	20.60	24.52	26.89	24.71	27.01	0.746	0.599	0.717	0.813	0.765	0.840	0.314	0.356	0.342	0.287	0.309	0.275
$L = 0, W = 256$	24.80	20.68	24.63	26.94	24.78	27.02	0.747	0.599	0.717	0.814	0.766	0.839	0.312	0.353	0.340	0.284	0.306	0.275
$L = 2, W = 64$	24.81	20.62	24.66	26.96	24.87	27.02	0.746	0.598	0.716	0.813	0.766	0.839	0.315	0.359	0.343	0.287	0.306	0.276
$L = 0, W = 16$	24.89	20.57	24.73	27.00	24.97	27.24	0.747	0.598	0.717	0.814	0.766	0.840	0.312	0.352	0.341	0.285	0.306	0.275
$L = 0, W = 32$	24.91	20.58	24.80	27.06	24.98	27.19	0.746	0.596	0.716	0.813	0.765	0.840	0.314	0.356	0.343	0.287	0.308	0.276
$L = 0, W = 64$	24.96	20.64	24.87	27.02	25.02	27.33	0.747	0.599	0.717	0.813	0.766	0.841	0.312	0.353	0.340	0.285	0.305	0.274
$L = 2, W = 16$	24.97	20.65	24.79	27.08	25.05	27.33	0.747	0.599	0.717	0.815	0.767	0.841	0.312	0.356	0.340	0.284	0.304	0.273
$L = 0, W = 128$	24.97	20.65	24.75	27.11	25.03	27.39	0.747	0.599	0.717	0.815	0.767	0.841	0.311	0.353	0.340	0.284	0.304	0.273
$L = 1, W = 32$	25.02	20.67	24.83	27.10	25.12	27.43	0.748	0.600	0.717	0.815	0.767	0.841	0.310	0.351	0.340	0.283	0.304	0.272
$L = 1, W = 64$	25.03	20.73	24.85	27.13	25.13	27.39	0.748	0.602	0.717	0.816	0.766	0.840	0.311	0.353	0.340	0.282	0.304	0.273
$L = 0, W = 192$	25.04	20.61	24.91	27.21	25.14	27.37	0.748	0.600	0.718	0.815	0.768	0.842	0.311	0.353	0.340	0.283	0.305	0.273
$L = 1, W = 128$	25.04	20.68	24.93	27.22	25.10	27.36	0.749	0.602	0.719	0.816	0.768	0.841	0.310	0.353	0.339	0.283	0.304	0.273

Table S.T9. Combination of different positional encoding. Either encoding on the splat position (PE) or the normalized viewing direction (DE). The available frequencies are either [5] or [10] and [0] indicates the plain vector with no encoding. The colors indicate the **best** and **worst** results.

	PSNR (\uparrow)						SSIM (\uparrow)						LPIPS (\downarrow)					
	All	RGB	G	R	RE	NIR	All	RGB	G	R	RE	NIR	All	RGB	G	R	RE	NIR
PE[0]	24.48	20.04	24.45	26.64	24.55	26.79	0.739	0.584	0.710	0.807	0.760	0.836	0.326	0.375	0.355	0.297	0.317	0.284
PE[10]	24.57	20.14	24.45	26.70	24.74	26.89	0.743	0.590	0.713	0.810	0.763	0.837	0.322	0.367	0.351	0.293	0.316	0.284
PE[5]	24.62	20.28	24.50	26.67	24.68	27.04	0.743	0.593	0.713	0.809	0.763	0.838	0.320	0.366	0.349	0.291	0.312	0.281
None	25.02	20.67	24.83	27.10	25.12	27.43	0.748	0.600	0.717	0.815	0.767	0.841	0.310	0.351	0.340	0.283	0.304	0.272
PE[0]-DE[0]	25.09	20.83	24.90	27.20	25.15	27.44	0.753	0.610	0.724	0.820	0.772	0.843	0.307	0.353	0.336	0.278	0.299	0.268
PE[5]-DE[5]	25.12	20.65	24.95	27.16	25.27	27.65	0.747	0.599	0.718	0.814	0.765	0.840	0.314	0.360	0.344	0.285	0.306	0.274
PE[10]-DE[10]	25.17	20.63	24.99	27.27	25.28	27.73	0.746	0.597	0.716	0.813	0.764	0.838	0.316	0.365	0.345	0.287	0.307	0.276
DE[5]	25.23	20.65	25.01	27.41	25.34	27.80	0.746	0.599	0.716	0.814	0.765	0.840	0.313	0.359	0.343	0.284	0.304	0.272
DE[10]	25.29	20.83	25.06	27.40	25.45	27.78	0.745	0.597	0.715	0.813	0.763	0.838	0.315	0.363	0.344	0.286	0.307	0.275
DE[0]	25.29	20.86	25.12	27.29	25.45	27.82	0.754	0.612	0.724	0.820	0.771	0.843	0.304	0.347	0.333	0.276	0.296	0.265

Table S.T10. Comparison on GARDEN scene. The colors indicate the **best** and **second best** results.

	PSNR (\uparrow)						SSIM (\uparrow)						LPIPS (\downarrow)					
	All	RGB	G	R	RE	NIR	All	RGB	G	R	RE	NIR	All	RGB	G	R	RE	NIR
ThermalGaus. (W)	26.10	23.45	26.30	25.06	28.95	26.72	0.739	0.690	0.732	0.717	0.795	0.762	0.315	0.290	0.309	0.294	0.329	0.351
ThermoNeRF (W)	22.91	18.72	23.51	21.27	26.93	24.10	0.589	0.371	0.615	0.555	0.704	0.700	0.438	0.457	0.433	0.436	0.439	0.426
3DGS (O)	26.91	23.47	26.85	26.19	29.38	28.69	0.777	0.692	0.747	0.775	0.825	0.843	0.270	0.217	0.281	0.235	0.313	0.303
ThermalGaus. (O)	27.14	23.14	27.19	26.13	30.05	29.20	0.761	0.646	0.742	0.759	0.824	0.833	0.315	0.305	0.326	0.299	0.326	0.316
Ours (O)	27.44	23.11	27.53	26.64	30.36	29.56	0.779	0.676	0.750	0.782	0.837	0.849	0.255	0.251	0.266	0.241	0.264	0.254

Table S.T11. Comparison on SINGLE TREE scene. The colors indicate the **best** and **second best** results.

	PSNR (\uparrow)						SSIM (\uparrow)						LPIPS (\downarrow)					
	All	RGB	G	R	RE	NIR	All	RGB	G	R	RE	NIR	All	RGB	G	R	RE	NIR
ThermalGaus. (W)	22.49	18.32	23.36	24.20	23.06	23.51	0.667	0.428	0.678	0.746	0.715	0.767	0.395	0.411	0.380	0.340	0.381	0.460
ThermoNeRF (W)	17.25	14.03	17.66	18.00	17.22	19.35	0.477	0.144	0.522	0.573	0.511	0.633	0.695	0.793	0.689	0.673	0.671	0.648
3DGS (O)	22.53	19.38	22.07	23.44	22.36	25.41	0.677	0.490	0.598	0.731	0.712	0.853	0.359	0.263	0.378	0.372	0.357	0.427
ThermalGaus. (O)	22.28	17.38	21.96	23.27	22.72	26.06	0.644	0.375	0.602	0.722	0.691	0.831	0.405	0.435	0.446	0.385	0.385	0.372
Ours (O)	25.56	20.13	24.81	26.67	26.31	29.87	0.731	0.521	0.664	0.804	0.781	0.884	0.271	0.297	0.315	0.256	0.245	0.242

Table S.T12. Comparison on LAKE scene. The colors indicate the **best** and **second best** results.

	PSNR (\uparrow)						SSIM (\uparrow)						LPIPS (\downarrow)					
	All	RGB	G	R	RE	NIR	All	RGB	G	R	RE	NIR	All	RGB	G	R	RE	NIR
ThermalGaus. (W)	21.03	20.02	21.44	24.19	19.63	19.86	0.698	0.567	0.720	0.801	0.676	0.725	0.393	0.475	0.411	0.343	0.380	0.359
ThermoNeRF (W)	16.62	16.13	17.37	20.38	14.51	14.70	0.554	0.440	0.609	0.721	0.498	0.504	0.671	0.792	0.664	0.591	0.660	0.646
3DGS (O)	21.16	20.76	20.88	24.63	19.54	20.01	0.658	0.587	0.616	0.764	0.627	0.696	0.459	0.500	0.518	0.467	0.407	0.402
ThermalGaus. (O)	21.77	20.99	22.23	25.44	19.69	20.50	0.677	0.610	0.667	0.782	0.624	0.701	0.435	0.492	0.462	0.395	0.435	0.389
Ours (O)	22.53	21.58	23.14	26.13	20.46	21.34	0.711	0.636	0.695	0.806	0.672	0.744	0.386	0.457	0.416	0.346	0.382	0.331

Table S.T13. Comparison on FRUIT TREES scene. The colors indicate the **best** and **second best** results.

	PSNR (\uparrow)						SSIM (\uparrow)						LPIPS (\downarrow)					
	All	RGB	G	R	RE	NIR	All	RGB	G	R	RE	NIR	All	RGB	G	R	RE	NIR
ThermalGaus. (W)	20.85	16.12	21.46	23.78	20.08	22.81	0.560	0.425	0.535	0.645	0.551	0.646	0.409	0.418	0.421	0.386	0.412	0.406
ThermoNeRF (W)	19.38	15.02	20.74	22.43	17.59	21.13	0.479	0.243	0.497	0.608	0.447	0.599	0.506	0.549	0.519	0.473	0.518	0.474
3DGS (O)	20.92	16.69	21.02	22.89	20.37	23.61	0.603	0.487	0.535	0.654	0.603	0.739	0.323	0.280	0.354	0.351	0.311	0.321
ThermalGaus. (O)	21.66	16.42	22.14	24.50	21.02	24.21	0.625	0.443	0.590	0.711	0.629	0.753	0.327	0.359	0.357	0.312	0.317	0.289
Ours (O)	22.90	17.42	23.16	26.07	22.21	25.64	0.668	0.506	0.624	0.752	0.675	0.785	0.269	0.301	0.301	0.254	0.257	0.231

Table S.T14. Comparison on GOLF scene. The colors indicate the **best** and **second best** results.

	PSNR (\uparrow)						SSIM (\uparrow)						LPIPS (\downarrow)					
	All	RGB	G	R	RE	NIR	All	RGB	G	R	RE	NIR	All	RGB	G	R	RE	NIR
ThermalGaus. (W)	28.70	22.21	29.39	31.87	29.56	30.46	0.780	0.551	0.833	0.885	0.819	0.812	0.355	0.448	0.314	0.278	0.340	0.394
ThermoNeRF (W)	24.04	18.06	24.85	25.05	24.24	28.02	0.602	0.270	0.706	0.750	0.652	0.633	0.711	0.994	0.652	0.575	0.701	0.634
3DGS (O)	27.62	24.98	26.04	28.89	26.43	31.77	0.812	0.710	0.782	0.856	0.807	0.904	0.431	0.303	0.497	0.478	0.455	0.424
ThermalGaus. (O)	29.72	24.02	29.59	31.10	29.76	34.60	0.806	0.591	0.826	0.885	0.820	0.921	0.425	0.553	0.419	0.353	0.440	0.350
Ours (O)	31.96	25.24	32.29	33.87	32.77	36.04	0.856	0.699	0.863	0.911	0.871	0.945	0.267	0.360	0.277	0.224	0.257	0.213

Table S.T15. Comparison on BUD SWELLING scene. The colors indicate the **best** and **second best** results.

	PSNR (\uparrow)						SSIM (\uparrow)						LPIPS (\downarrow)					
	All	RGB	G	R	RE	NIR	All	RGB	G	R	RE	NIR	All	RGB	G	R	RE	NIR
ThermalGaus. (W)	23.24	18.25	23.23	25.90	24.00	24.82	0.699	0.586	0.686	0.770	0.731	0.724	0.298	0.290	0.307	0.293	0.271	0.327
ThermoNeRF (W)	17.16	12.81	17.83	20.59	16.26	18.33	0.397	0.124	0.433	0.599	0.388	0.443	0.698	0.800	0.699	0.669	0.668	0.652
3DGS (O)	22.95	19.59	21.10	24.60	23.10	26.35	0.709	0.658	0.601	0.743	0.727	0.818	0.263	0.182	0.322	0.334	0.235	0.241
ThermalGaus. (O)	23.17	18.55	22.18	25.89	23.08	26.14	0.710	0.577	0.645	0.796	0.725	0.808	0.266	0.271	0.319	0.269	0.245	0.228
Ours (O)	25.11	19.93	23.77	27.75	25.13	28.95	0.766	0.654	0.696	0.843	0.781	0.856	0.205	0.213	0.253	0.206	0.183	0.168

Table S.T16. Comparison on SOLAR scene. The colors indicate the **best** and **second best** results.

	PSNR (\uparrow)						SSIM (\uparrow)						LPIPS (\downarrow)					
	All	RGB	G	R	RE	NIR	All	RGB	G	R	RE	NIR	All	RGB	G	R	RE	NIR
ThermalGaus. (W)	22.42	20.33	22.72	24.62	21.19	23.25	0.754	0.705	0.784	0.780	0.732	0.766	0.230	0.264	0.212	0.200	0.237	0.238
ThermoNeRF (W)	14.98	12.94	14.41	16.65	14.72	16.16	0.404	0.196	0.409	0.507	0.400	0.509	0.520	0.671	0.483	0.458	0.493	0.497
3DGS (O)	23.24	21.17	22.45	25.99	22.17	24.42	0.809	0.735	0.793	0.857	0.808	0.852	0.231	0.234	0.248	0.204	0.237	0.234
ThermalGaus. (O)	23.49	20.67	22.97	26.31	22.69	24.82	0.804	0.707	0.791	0.859	0.810	0.853	0.236	0.292	0.251	0.189	0.238	0.212
Ours (O)	24.05	20.82	23.23	27.41	23.30	25.49	0.831	0.737	0.812	0.893	0.841	0.875	0.206	0.260	0.224	0.156	0.207	0.184

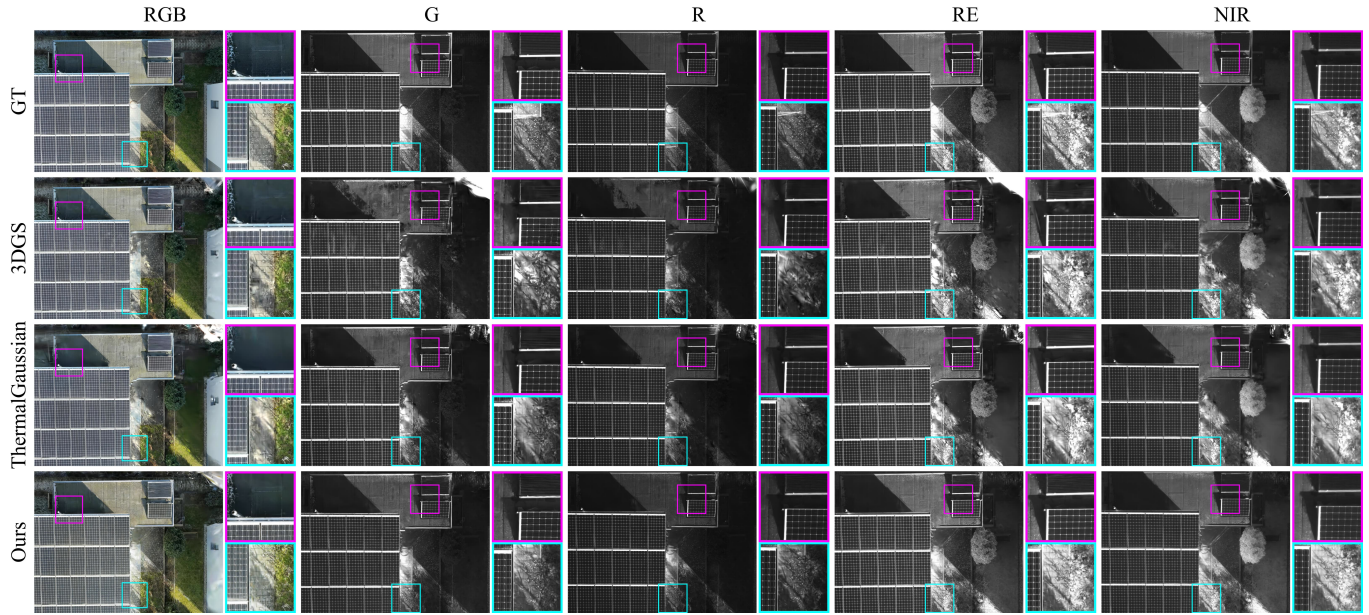


Fig. S.F2. Visual comparison on the SOLAR scene with all available spectral-bands. The used ThermalGaussian method in this comparison is our multi-spectral re-implementation.

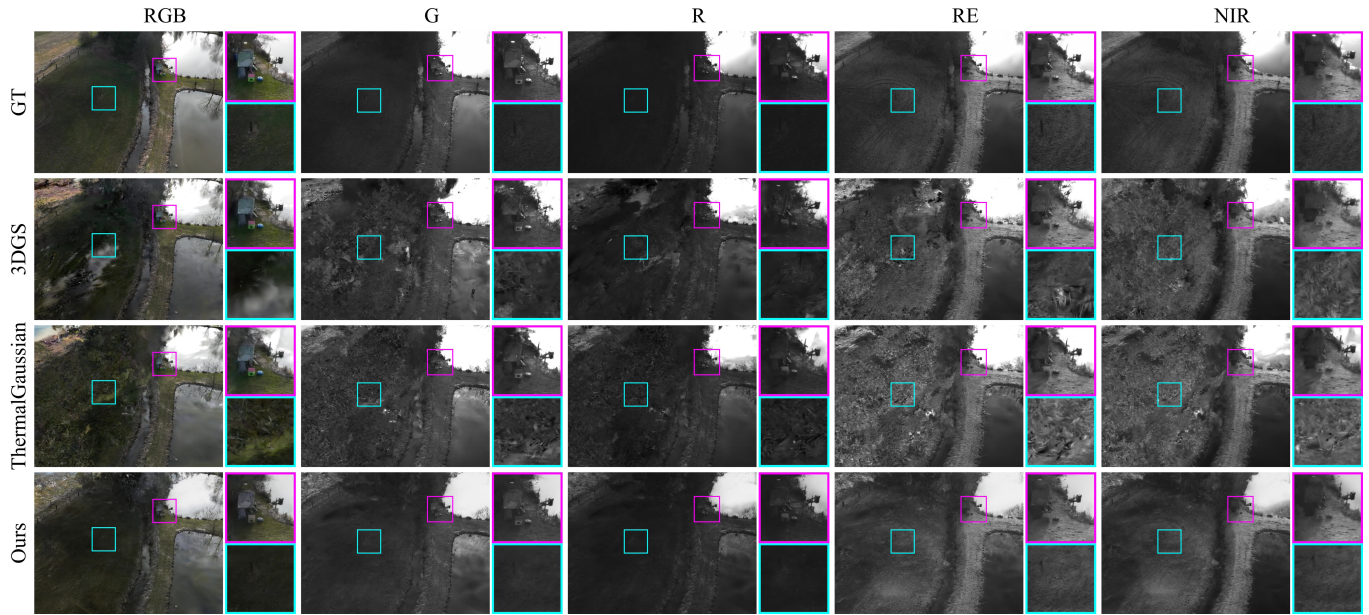


Fig. S.F3. Visual comparison on the LAKE scene with all available spectral-bands. The used ThermalGaussian method in this comparison is our multi-spectral re-implementation.

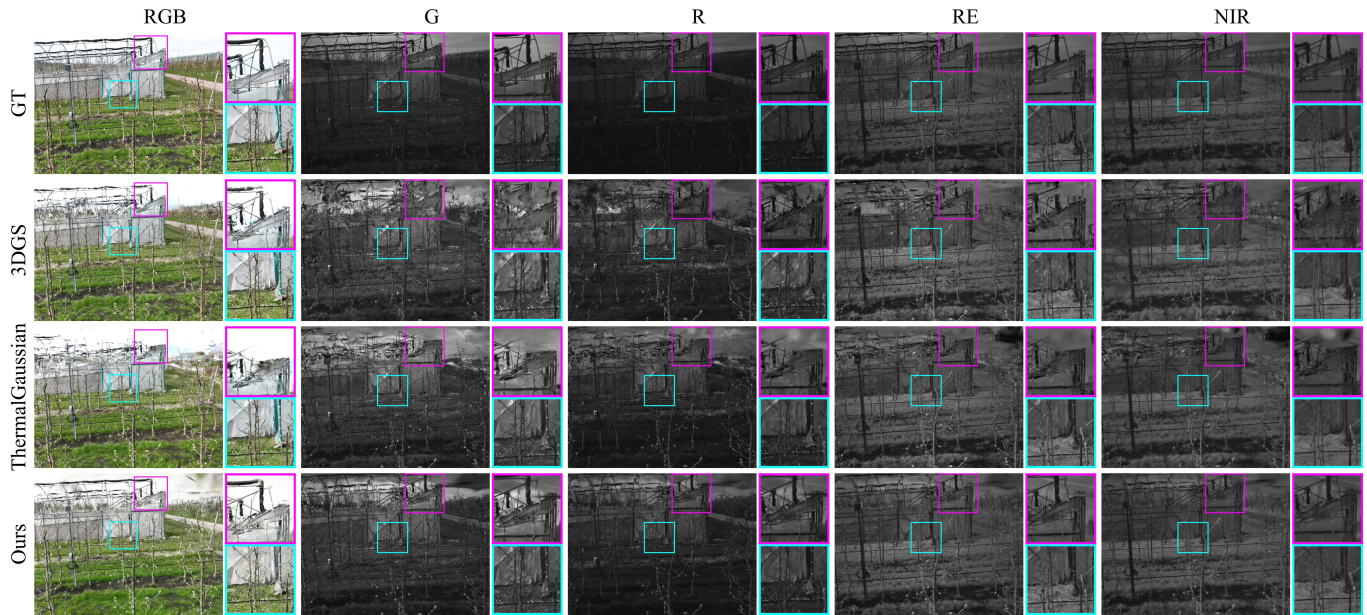


Fig. S.F4. Visual comparison on the BUD SWELLING scene with all available spectral-bands. The used ThermalGaussian method in this comparison is our multi-spectral re-implementation.

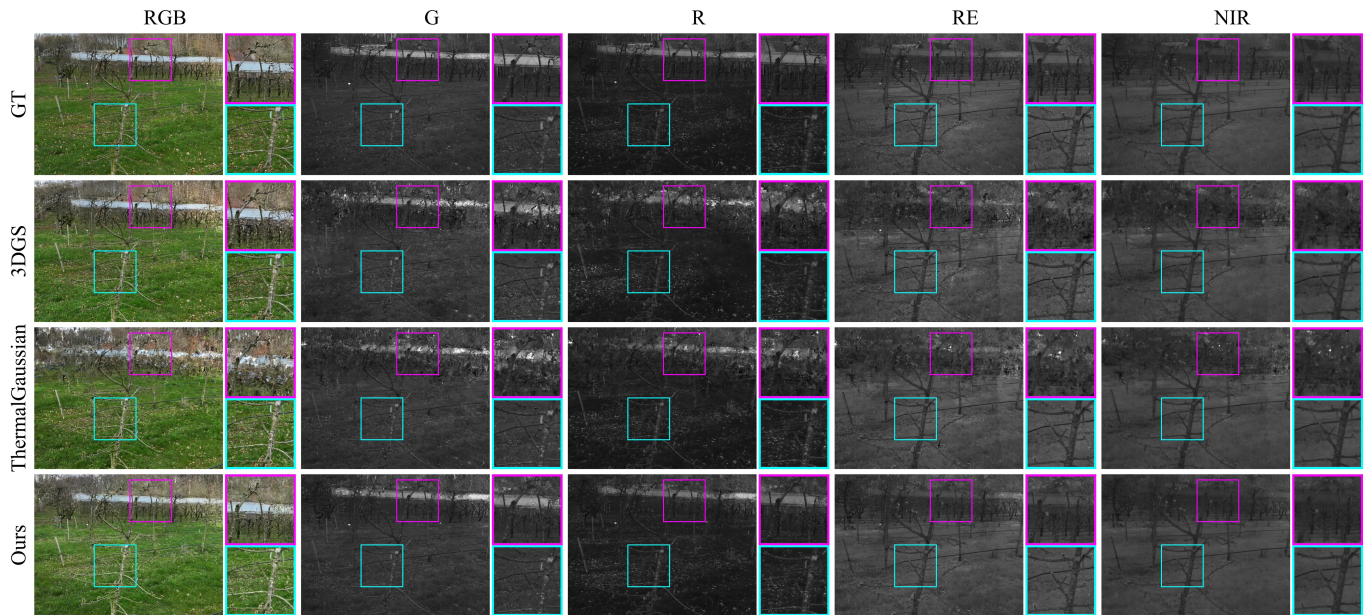


Fig. S.F5. Visual comparison on the SINGLE TREE scene with all available spectral-bands. The used ThermalGaussian method in this comparison is our multi-spectral re-implementation.